



Structural constraints of induced earthquakes in the Weiyuan Shale Gas Field revealed by high-resolution body-wave tomography and earthquake relocation

Jinping Zi^a, Hongfeng Yang^{a,b,*}, Jinrong Su^c, Liang Chen^d

^a Earth and Environmental Sciences Programme, The Chinese University of Hong Kong, Hong Kong, China

^b Shenzhen Research Institute, The Chinese University of Hong Kong, Shenzhen, China

^c Earthquake Monitoring Center, Sichuan Earthquake Administration, China

^d China University of Petroleum, Beijing, China

ARTICLE INFO

Keywords:

Induced earthquake
Tomography
Structural deformation
Weiyuan Shale Gas Field

ABSTRACT

Increasing concerns have been raised about hydraulic fracturing (HF) due to its capability of triggering damaging earthquakes. Although there is a common consensus that local geological settings play significant roles in these earthquakes, to what extent they influence earthquake locations and magnitudes within a shale gas field remains unclear. Here we conduct body-wave travel time tomography, earthquake relocation, and structural analysis in the Weiyuan Shale Gas Field (WSGF), Sichuan Basin, China. We find that structural deformation of the Weiyuan anticline and the newly revealed basement rift constrained the locations and magnitudes of $M_L \geq 3.0$ earthquakes in the WSGF. We also observe that $M_L \geq 3.0$ earthquakes are more prone to occur in low-velocity or velocity transition zones that are geologically susceptible. Based on high-resolution earthquake locations, we use aftershocks to delineate the fault plane of the largest M_w 5.0 in the WSGF. Our analysis shows the M_w 5.0 event nucleated in the basement rift and ruptured a fault plane strikes along northeast. Our results shed light on mitigating destructive earthquakes in shale gas fields by identifying geologically susceptible zones using structural deformation simulation and high-resolution tomography methods.

1. Introduction

Anthropogenic activities, such as waste-water injection (Ellsworth, 2013; Keranen et al., 2013), geothermal development (Grigoli et al., 2018; Kim et al., 2018), natural gas storage (Jiang et al., 2020; Zhou et al., 2019), and shale gas production (Bao and Eaton, 2016), could lead to damaging earthquakes (Ellsworth, 2013; Grigoli et al., 2017; Yang et al., 2017). In recent years, increasing concerns have been raised about hydraulic fracturing (HF) because plenty of moderate magnitude earthquakes ($M \geq 4.0$) were reported to relate to HF activities, such as in the Sichuan Basin, China, including shale gas fields in Weiyuan (Yang et al., 2020; Lei et al., 2020; Wang et al., 2020; Sheng et al., 2020), Luzhou, and Changning (Fig. 1a; Lei et al., 2020), the Western Canada Sedimentary Basin (Mahani et al., 2017; Eyre et al., 2019), and the Eagle Ford Shale Play in the USA (Schultz et al., 2020). Therefore, it is critical to understand the influencing factors of these earthquakes.

HF-related (induced or triggered) earthquakes in different shale gas

fields present distinct characteristics. For example, Rubinstein and Babaie Mahani (2015) concluded that shale gas production plays a limited role in the seismicity increase in Oklahoma, USA. In the Western Canada Sedimentary Basin, only a limited quantity of fracking wells generated sensible earthquakes ($M \geq 3$) even though the reported maximum magnitude reached M_w 4.6 (Atkinson et al., 2020; Mahani et al., 2017). In the Sichuan Basin, earthquakes are intense (Lei et al., 2020), with maximum magnitudes achieved M_L 5.7 and M_s 6.0 (Lei et al., 2019; Zhao et al., 2023). It is therefore inferred that tectonic settings influence the occurrence of HF-related earthquakes (Schultz et al., 2020; Atkinson et al., 2020; Lei et al., 2020; Kao et al., 2018). For example, Wang et al. (2022) related the frequent occurrence of three $M_w \geq 4.0$ events in the Changning Shale Gas Field, Sichuan Basin, to its position in a triple junction region near the southeastern margin of the Tibetan Plateau. However, how underground structures vary within a shale gas field and influence locations and magnitudes of earthquakes remain unclear. Knowledge concerning the above question is not only important

* Corresponding author at: Earth and Environmental Sciences Programme, The Chinese University of Hong Kong, Hong Kong, China.

E-mail address: hyang@cuhk.edu.hk (H. Yang).

<https://doi.org/10.1016/j.tecto.2023.230007>

Received 6 December 2022; Received in revised form 2 June 2023; Accepted 9 August 2023

Available online 19 August 2023

0040-1951/© 2023 Elsevier B.V. All rights reserved.

for seismic hazard mitigation but also critical in advancing our understanding of HF-related earthquakes.

The Weiyuan Shale Gas Field (WSGF), which is located in the southwestern Sichuan Basin and preserves the largest shale gas volume in China (China Energy Administration) (Fig. 1a), experienced eight $M_w \geq 4.0$ earthquakes since massive fracking started in 2015 (Table 1; Fig. 1b, c), leading to severe damage to residents and properties. The two largest events, the M_w 5.0 and the M_w 4.9, are located in the north-eastern Weiyuan, with relatively deep centroid depth (Table 1); the other six are located in the area close to the Molin fault, which is a tear fault of the Weiyuan anticline (Table 1; Fig. 1b; Wang et al., 2020). However, it remains unclear why the frequency, depths, and moment releases of $M_w \geq 4.0$ earthquakes exhibit such contrasting differences. Besides, there also occurred a large number of felt $M_L \geq 3.0$ events, which could lead to possible social panic. Therefore, understanding the controlling factors of these earthquakes is important for earthquake hazard mitigation and relieving serious social concerns.

Furthermore, the seismogenic mechanisms and responsible faults of the largest earthquakes in the WSGF remain controversial, as various centroid depths were reported using different velocity models (Wang

et al., 2020; Yi et al., 2020; Sheng et al., 2020; Lei et al., 2020). For example, the September 2019 M_w 5.0 earthquake was inferred to occur on a low-angle (33°) southeast-dipping back-thrust fault with a centroid depth of 5.0 km by Wang et al. (2020), which is similar to Yi et al. (2020)'s focal mechanism result with a depth of 4.5 km. Lei et al. (2020) reported a similar dip angle of the fault plane. However, the centroid depth was much shallower, 2.48 km. Furthermore, Sheng et al. (2020) presented a centroid depth of 2.9 km and inferred from rupture directivity analysis that the responsible fault oriented at 201° with a high dip angle of 68° toward northwest. These controversial results lead to difficulties in revealing the triggering mechanism of this destructive event (Table 1). The accurate hypocenters and the distribution of aftershocks could be applied to constrain the corresponding fault plane (e.g., Yang et al., 2009), which may shed light on this unresolved significant question.

Addressing the questions above relies heavily on high-resolution earthquake locations and subsurface structural information. Tomography methods, which invert for subsurface velocities, have been widely used to identify underground geological structures, e.g., in plate boundaries (Guo et al., 2018; Guo et al., 2021; Zhu et al., 2021) and

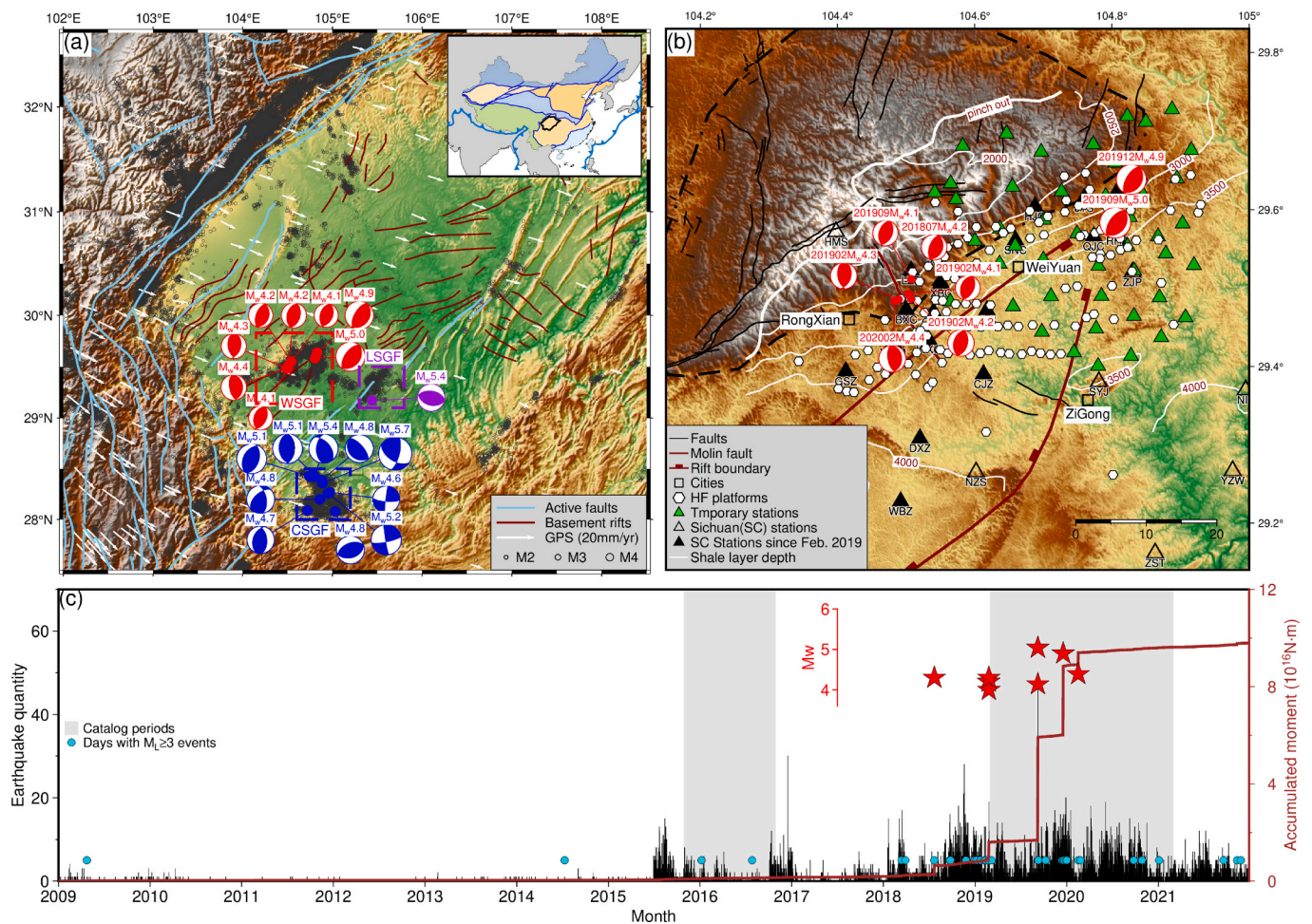


Fig. 1. Research background of the Weiyuan shale gas field (WSGF). (a) Topography map of the Sichuan Basin with active faults (Zhang et al., 2013), basement rifts (Hu et al., 2022), seismicity from January 2009 to December 2021 (China Earthquake Data Center, <https://data.earthquake.cn>), GPS velocities (Wang and Shen, 2020) and focal mechanisms of $M_w \geq 4.0$ (Yang et al., 2020; Yi et al., 2020; Lei et al., 2019; Lei et al., 2020; IRIS) in the Weiyuan (WSGF), Changning (CSGF), and Luzhou (LSGF) shale gas field shown. (b) Topography map of the WSGF with faults, hydraulic fracturing platforms, target shale layer buried depths (Ma et al., 2020), and seismic networks shown. Empty black triangles, solid black triangles, and solid green triangles represent the long-term Sichuan network stations, newly deployed Sichuan network stations since the February 2019 M_w 4.3 event, and the temporary stations deployed from 2015 to 2016. The black dashed line indicates the boundary of the Weiyuan anticline on the surface, across which surface elevation increased tremendously. (c) Plot of day earthquake quantities and accumulated seismic moment in the WSGF using the empirical conversion equation between M_w and M_L from Yi et al. (2020). Days with $M_L \geq 3.0$ events are highlighted by cyan dots. Occurrence times of 8 $M_w \geq 4.0$ events in the WSGF are marked by red stars. The two shadowed areas denote the time periods of the two earthquake catalogs used in this study. (For interpretation of the references to colour in this figure legend, the reader is referred to the web version of this article.)

Table 1

Focal mechanisms and centroid depths of the 8 $M_w \geq 4.0$ earthquakes in the WSGF since 2015, when massive shale gas production started. The M_w 5.0 and the M_w 4.9 occurred in the northeastern Weiyuan with deeper depths. The other six are in the Molin area with shallower depths. ^a(Yi et al., 2020); ^b(Yang et al., 2020); ^c(Du et al., 2021); ^d(Wang et al., 2020); ^e(Lei et al., 2020); ^f(Sheng et al., 2020); ^g(this study)

Event date	M_w	M_L	Strike/Dip/ Rake (°)	Centroid depth (km)	Focal depth (km)
2018/07/ 23	4.2	4.5	20/32/90	1.5 ^a	–
2019/02/ 24	4.2	4.9	190/42/83	2.6 ^b	4.7 ^b
2019/02/ 25	4.0	4.7	15/47/90	2.5 ^a	3.9 ^b
			202/43/90	2.9 ^b	
			25/49/95	2.5 ^a	
2019/02/ 25	4.3	5.2	170/51/72	1.3 ^b	3.8 ^b
			13/29/92	2.0 ^a	
2019/09/ 08	5.0	5.6	40/32/94	4.5 ^a	6.2 ^c
			60/33/127	5.0 ^d	5.5 ^g
			25/39/70	2.5 ^e	
			201/68/75	2.9 ^f	
2019/09/ 08	4.1	4.6	24/44/96	2.0 ^a	2.4 ^g
2019/12/ 18	4.9	5.4	35/29/94	4.0 ^a	5.7 ^g
2020/02/ 16	4.4	4.7	0/29/99	2.5 ^a	3.4 ^g

crustal fault zones. In the WSGF, ambient noise tomography (Zeng et al., 2020) and surface-wave tomography (Wei et al., 2022) using a temporary network deployed in northeast Weiyuan (Fig. 1b), and body-wave tomography with a horizontal resolution of $0.1^\circ \times 0.1^\circ$ (Du et al., 2021) using the Sichuan Earthquake Agency (SEA) network (Fig. 1b) have been conducted and the results revealed distinct lateral velocity variations. However, the limited network coverage of the temporary network and the large inter-station distance of the SEA network prohibit their capability in resolving high-resolution subsurface structures in the WSGF, respectively.

In this work, we conduct high-resolution body-wave tomography inversion to invert for 3-D velocity structures using selected events from both the SEA network and the temporary network deployed from November 2015 to November 2016 in the WSGF (Fig. 1b). Using the inverted velocity structures with a resolution of $0.05^\circ \times 0.05^\circ$, we conduct double-difference relocation of $\sim 32,000$ earthquakes from the SEA catalog for the period from March 2019 to February 2021 and obtain a catalog with unprecedented resolution. We then interpret tomography results and investigate the relationship between geological features and earthquake distribution, which provide critical insights into the structural constraints on HF-related seismicity.

2. Geological background and shale gas production

2.1. Geological setting

The WSGF is located in the southwestern Sichuan Basin, which is within the upper Yangtze block (Fig. 1a) with a rigid basement and a sedimentary cover consists of Ediacaran to middle Mesozoic marine deposits and late Triassic to Cenozoic terrestrial strata (Liu et al., 2021). In 830–745 Ma, an extensional tectonic environment characterized by magma intrusions widely developed in the Upper Yangtze block (Li et al., 2003). Consistent with the extensional tectonic setting in the basin peripheries, intense basement rift structures featuring magma intrusions and thick deposits are identified within the Sichuan Basin with a maximum thickness of sediments over 5 km (Fig. 1a; Hu et al., 2022; Gu

and Wang, 2014), including the newly reported one which extends its northeast counterpart to the WSGF (Hu et al., 2022; Fig. 1b). The length and width of the rift structure are ~ 89 km and ~ 23 km, respectively.

The Weiyuan anticline is dominantly controlled by a northwest-dipping deep thrust ramp in the basement and a southeast-dipping back-thrust fault rooted in the Cambrian base with a depth of ~ 5 km (Hubbard and Shaw, 2009; Wang et al., 2020; Jia et al., 2020). The structural deformation of the deep thrust leads to a large-scale dome-shaped structure in the Weiyuan area (Hubbard and Shaw, 2009) and shallow southeast-dipping back-thrust fault dominates the current surface deformation of the Weiyuan anticline (Hubbard and Shaw, 2009; Wang et al., 2020; Fig. 1b). The base of the Ediacaran, which marks the end of the late Neoproterozoic extensional setting, located around ~ 0.6 km below the Cambrian base in the Weiyuan area (Liang et al., 2019).

The target shale layers are the Upper Ordovician Wufeng formation and the Lower Silurian Longmaxi formation, with a buried depth from <2.0 km in the center of the Weiyuan anticline to >4.0 km in the southern and the southeastern area (Fig. 1b). The average thickness of good-quality shale layers for production is 35–40 m (Ma et al., 2020). Well-log measurements show a west-east direction of the current maximum horizontal stress (SH_{max}) in the WSGF, with a variation of around 15° at different sites (Chen et al., 2018; Ma et al., 2017). Such stress orientation is consistent with thrust focal mechanisms of $M_s \geq 3.0$ earthquakes in the region, which is dominated by NNE strikes (Yi et al., 2020).

2.2. HF platform distribution

Horizontal wells trajectories in the WSGF have an extending length of 1200–1800 m with strikes along N-S or NNW-SSE that is perpendicular to local maximum horizontal stress (Ma et al., 2017; Li et al., 2017). Given the limited knowledge concerning HF platform distribution in the WSGF, we identify shale gas platforms using high-resolution Google Earth images (Fig. 2). >120 shale gas platforms are recognized from Google Earth images (Fig. 1b; Fig. 2). We also confirmed the names of 48 platforms during our field visits in 2020 and 2021.

3. Earthquakes and monitoring network

Two earthquake datasets are used in this study. One is recorded by a temporary network deployed in northeast Weiyuan from November 2015 to November 2016 (Fig. 1b, c). The other one is constructed from permanent station records of the SEA network, which was expanded to deploy 23 more stations after the deadly February 2019 M_w 4.3 earthquake (Fig. 1b, c).

3.1. The catalog from the temporary network

The temporary network consists of 50 stations with an average inter-station spacing of ~ 5 km (Fig. 1b) and a sampling rate of 100 Hz. The deployment started in November 2015, and ended in November 2016, with most stations having good records before June 2016. Zhou et al. (2021) conducted earthquake detection using the high-performance machine-learning-based detector, PhaseNet (Zhu and Beroza, 2018). Picked phases were then associated into 79,395 earthquakes using the Rapid Earthquake Association and Location (REAL) method (Zhang et al., 2019). A set of local 1-D velocity models were refined, and the absolute earthquake locations were obtained by the VELEST program (Zhou et al., 2021). After location, event waveforms were first deconvolved of the instrument response and then convolved with the theoretical Wood-Anderson seismometer response to estimate the magnitude. The final catalog includes 69,229 events with magnitudes ranging from M_L -0.5 to 3.5, with a magnitude of completeness of M_L 0.0 (Table 2).

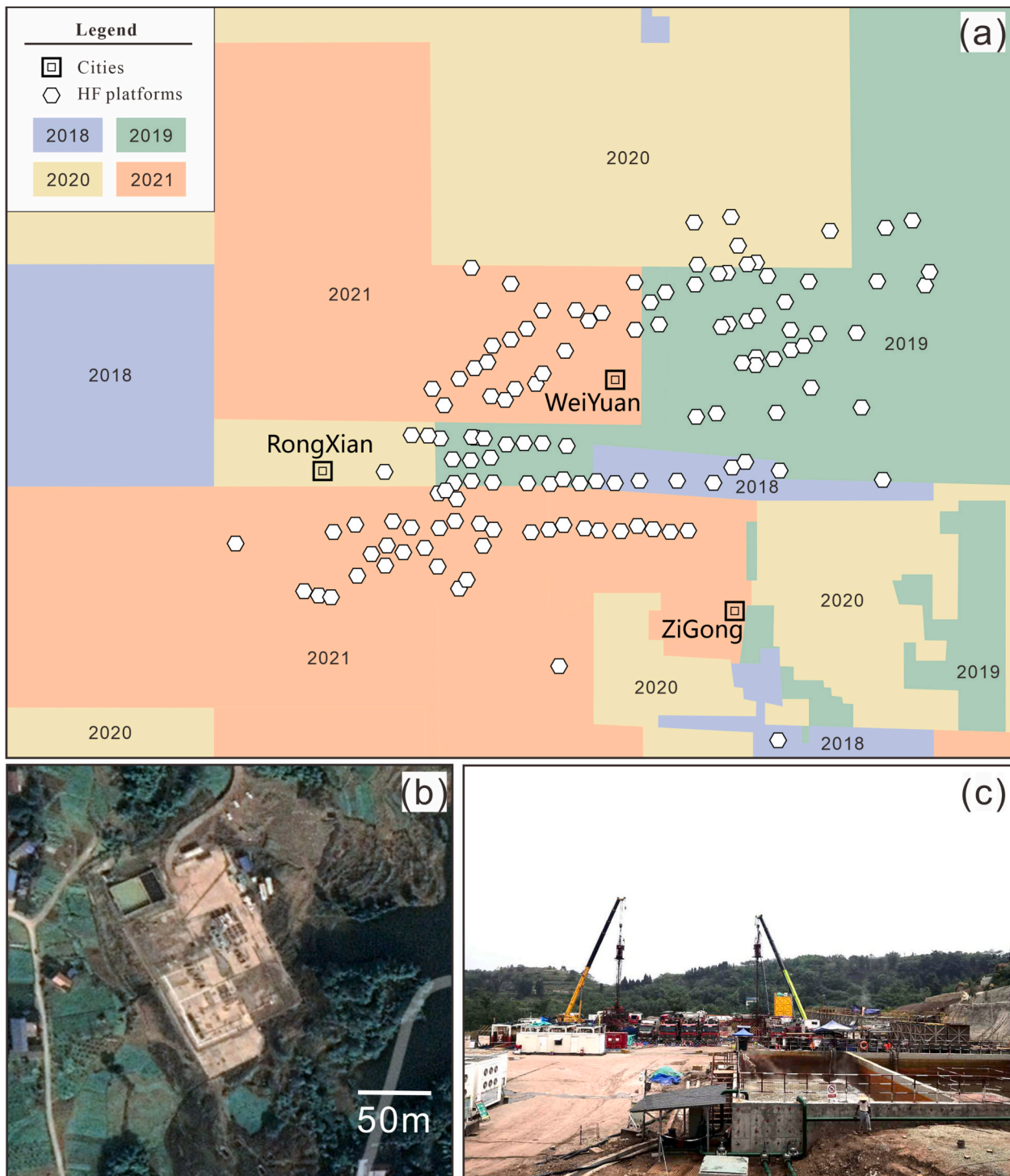


Fig. 2. Locations of hydraulic fracturing (HF) platforms identified using Google Earth images. (a) Map view of platform distribution with the background color showing the shot time of Google Earth images. (b, c) Google earth image (Jan. 2021) and on-site photo (Apr. 2020) of an example platform, W202H81.

3.2. The catalog from the SEA network

Since the occurrence of the shallow deadly M_w 4.3 Rongxian earthquake on 25th February 2019 with a centroid depth of ~ 1.3 km (Yang et al., 2020), the SEA network was enhanced by additional 23 stations, which leads to an improved inter-station distance from ~ 27 km to ~ 10 km (Fig. 1b). 32,253 events were recorded by the expanded network in the study region from 1st March 2019 to the end of 28th February 2021 (Fig. 3a), with a magnitude range of M_L 0.0 to M_w 5.0 and a magnitude completeness (M_c) of M_L 1.5 (Table 2).

4. Tomography inversion

We first update the absolute location for events in the SEA catalog using the HYPOINVERSE algorithm (Klein, 2002) with the local 1-D velocity models (Zhou et al., 2021). After relocation, earthquakes are mostly clustered in the Rongxian (west) and Weiyuan (east) counties (Fig. 3a). We then use the tomoDD method to invert for 3-D velocity models (Zhang and Thurber, 2006). In addition to differential travel times used to resolve source region velocities, we also include absolute travel times of stations in the inversion domain to resolve velocities

Table 2

Basic information about the two catalogs. The b value and the magnitude completeness (M_c) are calculated using the ZMAP software with a 95% self-similarity criteria.

Catalog	Quantity	Magnitude range	b value	M_c	Period
Temporary network	69,229	M_L -0.5 to 3.5	1.09	M_L 0.0	Nov. 2015 – Nov. 2016
SEA network	32,253	M_L 0.0 to M_w 5.0	1.07	M_L 1.5	Mar. 2019 – Feb. 2021

outside the source region (Fig. 3b).

4.1. Network coverage, velocity model, and earthquake selection

A total of 121 stations from the temporary and the SEA network are located within 200 km of the WSGF. To enhance the uniform distribution of earthquakes in the model, we apply a clockwise spherical rotation of 25° centered on (104.7° E, 29.5° N) to both earthquakes and stations, which leads to a good ray coverage in the longitude range of 104.3–105.0° E and the latitude range of 29.30–29.70°N (Fig. 3b). The horizontal distance between model velocity nodes is 0.05° in the center and increases to 0.1° in the peripheries (Fig. 3b); the vertical separation distance is 1 km for a focused depth range of 0–6 km and increases to 2 km and 6 km at greater depths (Table S1). Surface depth, which is set at 0 km, stands for the average elevation of stations.

Proper initial velocity models are critical for the inversion performance. Zhou et al. (2021) and Du et al. (2021) presented velocity models (V_p and V_s) in the WSGF by the temporary catalog and the SEA catalog using the VELEST and the tomoDD (0.1° × 0.1°) inversion, respectively. Their results are consistent in depths below 5 km and are distinct above 5 km (Fig. 4). To resolve the differences between the two sets of models, we conducted trial tomographic inversion sets from the 1-D velocity models derived from Du et al. (2021). A mean horizontal layer value change of >0.1 km/s will lead to an updated initial model. We then put the refined initial models as the input models for this study (Fig. 4).

Furthermore, the homogeneity of earthquake distribution also influences the model inversion capability. We first select events in the SEA catalog that were recorded by at least six stations. For earthquakes in the

temporary catalog, they need to be observed by at least 15 stations. However, selected events still show significant distribution heterogeneity (Fig. S1). The maximum quantity of earthquakes in one velocity grid is 8506, the mean value of earthquake quantities in grids that possess earthquakes is 104, and the median value is 7. Such prominent heterogeneity will inhibit the inversion stability. To resolve this, we set below criterias for further event selection to enhance inversion capability by excluding low-magnitude events, which tend to have large P-wave and S-wave arrival time uncertainties due to low signal-to-noise ratio:

- The target event quantity in one grid should be as close as 6 ($|N_{tmp} + N_{SEA} - 6|_{min}$).
- Under the above condition, the quantity difference between two catalogs should be minimized ($|N_{tmp} - N_{SEA}|_{min}$)

After event selection, 314 events from the temporary catalog and 1929 earthquakes from the SEA catalog are prepared for tomoDD inversion.

4.2. Differential times

After our event selection, there are total of 36,943 and 33,004 P-wave and S-wave arrival times. Their distance-time relationships exhibit apparent P and S wave velocities of 6.0 km/s and 3.5 km/s, respectively (Fig. S2). We first select the P and S phases by removing outliers with a misfit >5 s to theoretical values.

The separation distance in calculating differential times decides whether the velocity in the source region could be properly resolved (Guo and Zhang, 2017). The contribution of event pairs with a too-small separation distance to the inversion results is limited. Therefore, we set the maximum and minimum separation distances for catalog differential times calculation as 6.0 km and 0.1 km. The output average separation distance is 0.7 km.

To achieve better resolution in earthquake location than ordinary phase-picks, we conduct event waveform cross-correlation to measure differential times for events in the SEA catalog (Fig. S3) using the Sliding-window Cross-Correlation method (SCC; Yang et al., 2009). Event waveforms are cut and filtered with a bandpass range of 1–14 Hz

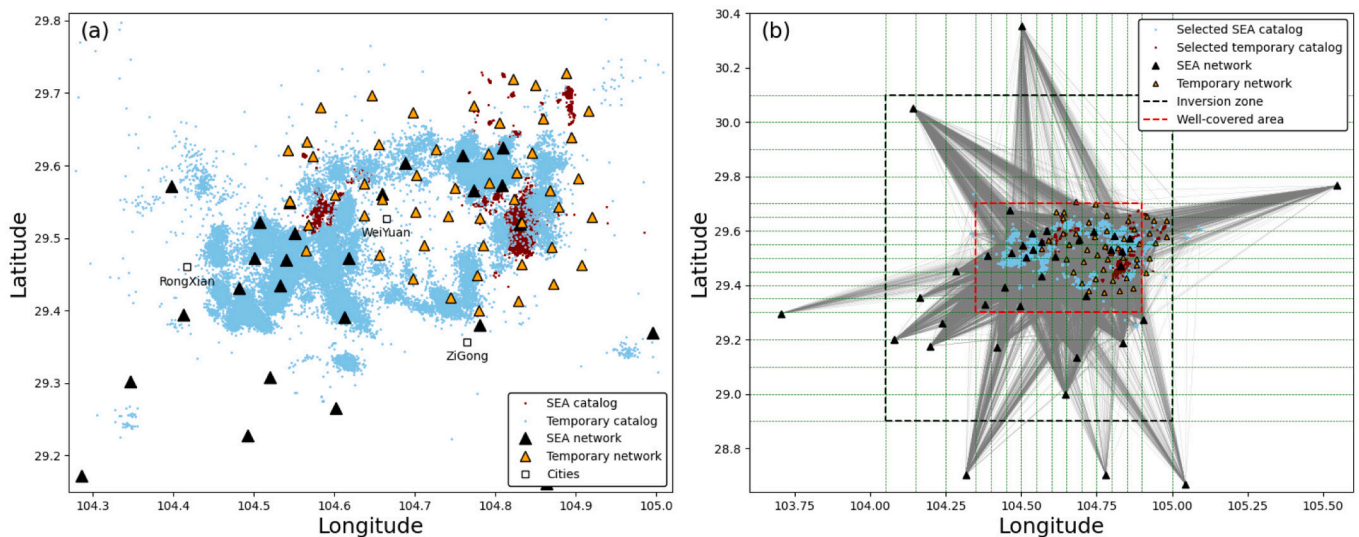


Fig. 3. Absolute earthquake locations (a) and the setup for tomoDD inversion (b). (a) Map view of the temporary network catalog (darkred) recorded by 50 temporary stations (orange) from November 2015 to November 2016 and the catalog (skyblue) recorded by the SEA network (black) from March 2019 to February 2021. (b) The inversion model setup with events and stations rotated 25° clockwise centered on (104.7°E, 29.5°N). Selected events and corresponding wave-propagation rays are shown. Intersections of green dashed lines indicate the velocity nodes. The grid spacing is 0.05° in the well-covered area and increases to 0.1° in the peripheries. (For interpretation of the references to colour in this figure legend, the reader is referred to the web version of this article.)

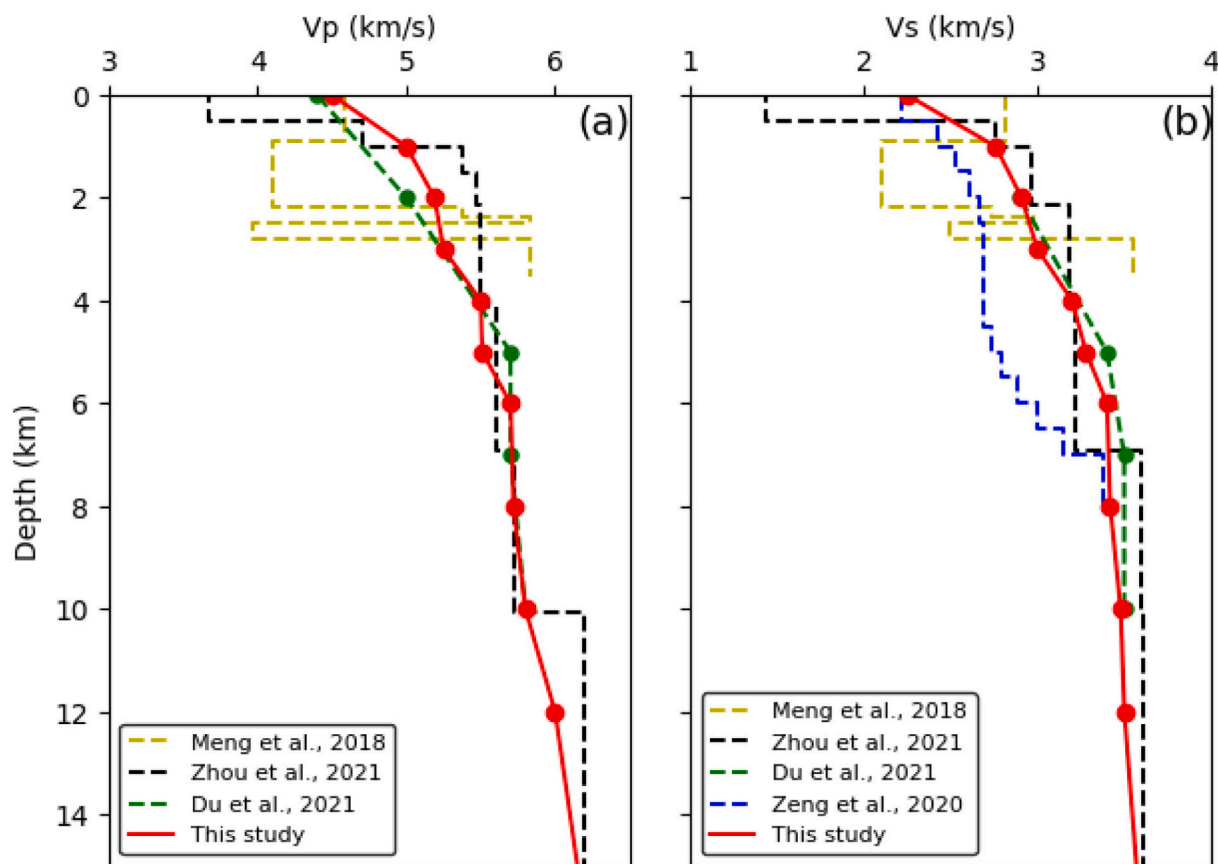


Fig. 4. Velocity models in the WSGF. Local VELEST velocity models (black dashed lines; Zhou et al., 2021) show distinct differences with local body-wave tomography velocity models (green dashed lines; Du et al., 2021) above 5 km. Trial inversions are conducted using Du et al. (2021)’s average 1-D models as initial input and update velocities for layers with an absolute mean velocity change of >0.1 km/s. The results are then taken as the input for this study (red solid lines). It is shown that the selected models are consistent with borehole data (Meng et al., 2018). Vs velocities constrained by ambient noise tomography (Zeng et al., 2020) are distinct from results constrained by body-wave arrivals. (For interpretation of the references to colour in this figure legend, the reader is referred to the web version of this article.)

to suppress noise. To calculate the cross-correlation coefficient, the time windows of a template waveform are set to be 0.7 s (0.05 s before and 0.65 s after) for the P wave and 2 s (0.1 s before and 1.9 s after) for the S wave. The maximum shift times are 0.1 s and 0.2 s for P and S, respectively. The SCC coefficient threshold is set to 0.7. A maximum epicenter threshold of 2 km and minimum observations from 4 stations are set to form an event-pair to ensure reliability. After that, the absolute travel times, the catalog differential times, and the waveform cross-correlation differential times are sent to the tomography inversion program (Table 3).

4.3. Inversion parameters

The damping and the smoothing factors during inversion are selected through the trade-off analysis (Fig. S4 a, b). In total, 6 iteration sets are conducted (Table S2) to invert for both velocity structures and earthquake locations. As velocities converge faster than earthquake locations, each joint inversion set is followed by one set that only relocates

Table 3
Absolute and differential travel times used in the tomoDD inversion.

Phase	Absolute travel times	Catalog differential times	Cross-correlation differential times
P	33,723	109,766	36,116
S	30,200	94,411	23,675

earthquakes.

In the first two iteration sets, we set high weights to absolute travel times to constrain absolute earthquake locations and velocity structures in the whole domain. In the next two iterations, we increase the weight of differential times to enhance the capability in refining relative locations and source region velocities. In the final two iteration sets, we put high weights on cross-correlation differential times to gain high-resolution earthquake locations and source velocity structures.

4.4. Resolution test

To verify the resolution of models, we conduct a checkerboard test (Fig. S5). 5% of positive and negative velocity perturbations are applied to the initial input V_p and V_s models. In the depth range of 1.0–6.0 km, most velocity nodes are well-recovered, showing satisfactory performance. Starting from 8 km, where few earthquakes occurred, the well-resolved area is confined to a smaller region due to the limited ray coverage.

Based on the checkerboard test, we quantify the resolvability of one velocity node following Zelt (1998)’s method,

$$R_i = \frac{\sum_{j=1}^M (\Delta V_j^i + \Delta V_j^i)^2}{2 \sum_{j=1}^M [(\Delta V_j^i)^2 + (\Delta V_j^i)^2]}$$

where M is the number of surrounding nodes around the node i, j indicates one surrounding node, ΔV_j^i is the input 5% velocity perturbation, ΔV_j^i denotes the recovered velocity perturbation. We use velocity nodes within a cube centered on node i and with a length of one grid interval along each dimension. A threshold of 0.7 is set to quantify the well-resolved nodes. Nodes with resolutions lower than the threshold are masked in the results.

5. Results

Our careful selection of initial input models and the application of waveform cross-correlation ensure the reliability of results. After the tomoDD inversion, we obtain well-refined V_p and V_s models with good resolution in 1–6 km depth (Fig. S5). The catalog differential times residual decreases from 0.47 s to 0.10 s, and the cross-correlation data

residual decreases from 0.096 s to 0.031 s (Fig. S4c), which are a 78.7% and a 67.7% reduction. In this part, we will introduce the results of earthquake relocation and inverted velocity models, including V_p , V_s , and V_p/V_s .

5.1. Earthquake relocation

We first refine the absolute locations of the SEA catalog using the input 1-D velocity models for tomography inversion. We then conduct double-difference relocation (Waldhauser and Ellsworth, 2000) using the updated 3-D velocity models from tomography inversion and receive a high-resolution earthquake catalog (Fig. 5). After six earthquake relocation iterations, the average pick and cross-correlation differential time residuals decrease from 0.155 s to 0.063 s and from 0.086 s to 0.014 s (Fig. S4d). 30,533 earthquakes are relocated. The average depth of events is 3.45 km, and 90% of events are located at the depth range of

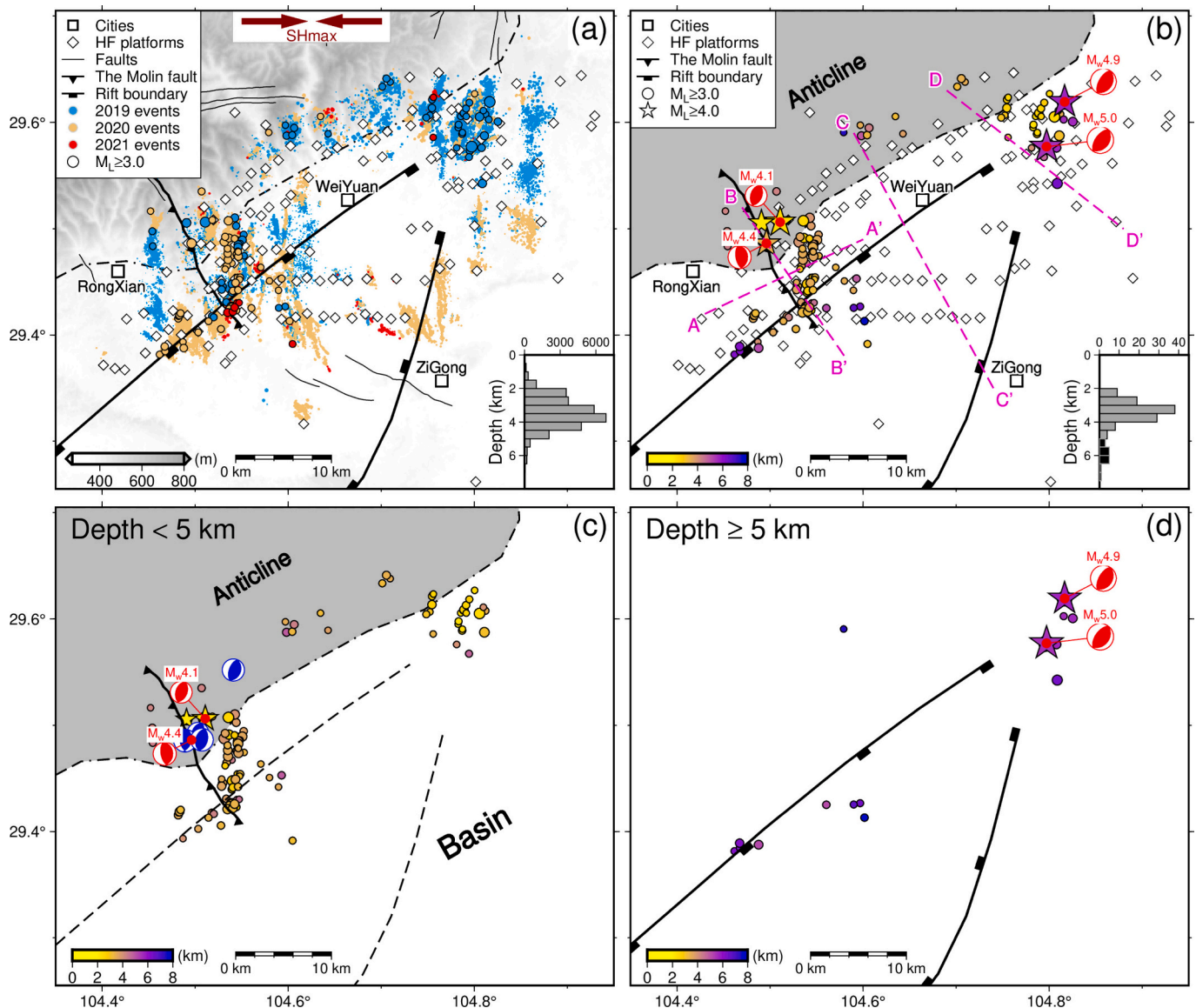


Fig. 5. Results of the double-difference earthquake relocation. (a) Locations of relocated SEA catalog. Earthquakes are colored by their occurrence years. The pair of red arrows indicate the current SH_{max} direction (Chen et al., 2018). (b) Locations of $M_L \geq 3.0$ (circles) and $M_L \geq 4.0$ (stars) events. Focal mechanisms of $M_w \geq 4.0$ events are shown. The depth histogram shows two concentrated groups for 2–5 km and 5–6.5 km, respectively. The four purple dashed lines indicate the traces of sections in Fig. 8 and Fig. 9. (c) Schematic plot showing locations of $M_L \geq 3.0$ events shallower than 5.0 km. The WeiYuan anticline is the dominant structure. Focal mechanisms in blue stand for $M_w \geq 4.0$ events that occurred before March 2019 since mid-2015 (Table. 1). (d) Schematic plot showing locations of $M_L \geq 3.0$ events deeper than 5.0 km. The basement rift is the dominant structure. (For interpretation of the references to colour in this figure legend, the reader is referred to the web version of this article.)

2–5 km.

We use the bootstrapping method to estimate relative location uncertainties (Efron, 1982; Efron and Tibshirani, 1991). Inversions are conducted using resampled catalog and cross-correlation differential times. From this process we can estimate the stability of results because observations from some stations are dropped during the resampling process. We conduct this process 100 times and the standard deviations of each event location are estimated to be the corresponding earthquake location uncertainty. We further exclude small-magnitude events ($M_L < 3$) obsessed with large standard errors (>500 m) in horizontal or depth. The mean average earthquake location standard errors for the final catalog are ~ 50 m in horizontal and ~ 80 m in depth. Location uncertainties are small in areas with dense and well-covered seismometer distribution and are relative high in areas with sparse or poor azimuthal coverage (Fig. S6).

Compared to scattered initial earthquake locations, relocated earthquakes are more linearized in clusters and are in proximity with nearby HF platforms (Fig. 5a). These lineations are consistent with local SH_{max} orientation and show differences regarding strikes of the basement rift, the Weiyuan anticline, surface faults, and $M_w \geq 4.0$ events (Fig. 5a). Therefore, we infer these lineations might either correspond to earthquakes induced by fracking directly or small-scale faults that are preferential to be reactivated under current SH_{max} direction. Detailed analysis of earthquake locations and horizontal well distribution would

be helpful to verify our inference.

Furthermore, earthquake occurrence times present distinct contrasts in different areas. Earthquakes in northeast Weiyuan mainly occurred in 2019 and dramatically decreased in 2020, indicating that massive fracking in northeastern Weiyuan ended in 2020. In the southwestern WSGF, a large number of earthquakes were recorded in 2019, 2020, and 2021, indicating intense fracking during the research period (Fig. 5a).

In contrast to the distribution of $M_L < 3.0$ events, which presents a strong correlation with locations of HF platforms, $M_L \geq 3.0$ events are concentrated in three areas: northeast Weiyuan, inside the Weiyuan anticline and the area close to the Molin fault (Fig. 5b). The depth histogram of $M_L \geq 3.0$ events shows a bimodal pattern with a separation distance of 5 km (Fig. 5b). For the domain shallower than 5 km, three $M_L \geq 4.0$ events occurred inside the Weiyuan anticline and $M_L \geq 3.0$ events are located in areas close to the anticline-basin boundary (Fig. 5c). For clusters far from the anticline, there is no $M_L \geq 3.0$ events recorded. For the domain deeper than 5 km, $M_L \geq 3.0$ events are mainly located inside the basement rift region and the area to its northeast, including the largest M_w 5.0 and M_w 4.9 (Fig. 5d; Table 1).

An earthquake density map is plotted to reveal the earthquake productivity (Fig. 6). Earthquakes are first gridded into grids with a size of $0.001^\circ \times 0.001^\circ$ and then smoothed by an average matrix with a dimension of 9×9 . The result shows that the highest earthquake productivity zones are in the Shuangshi town and northeast Weiyuan,

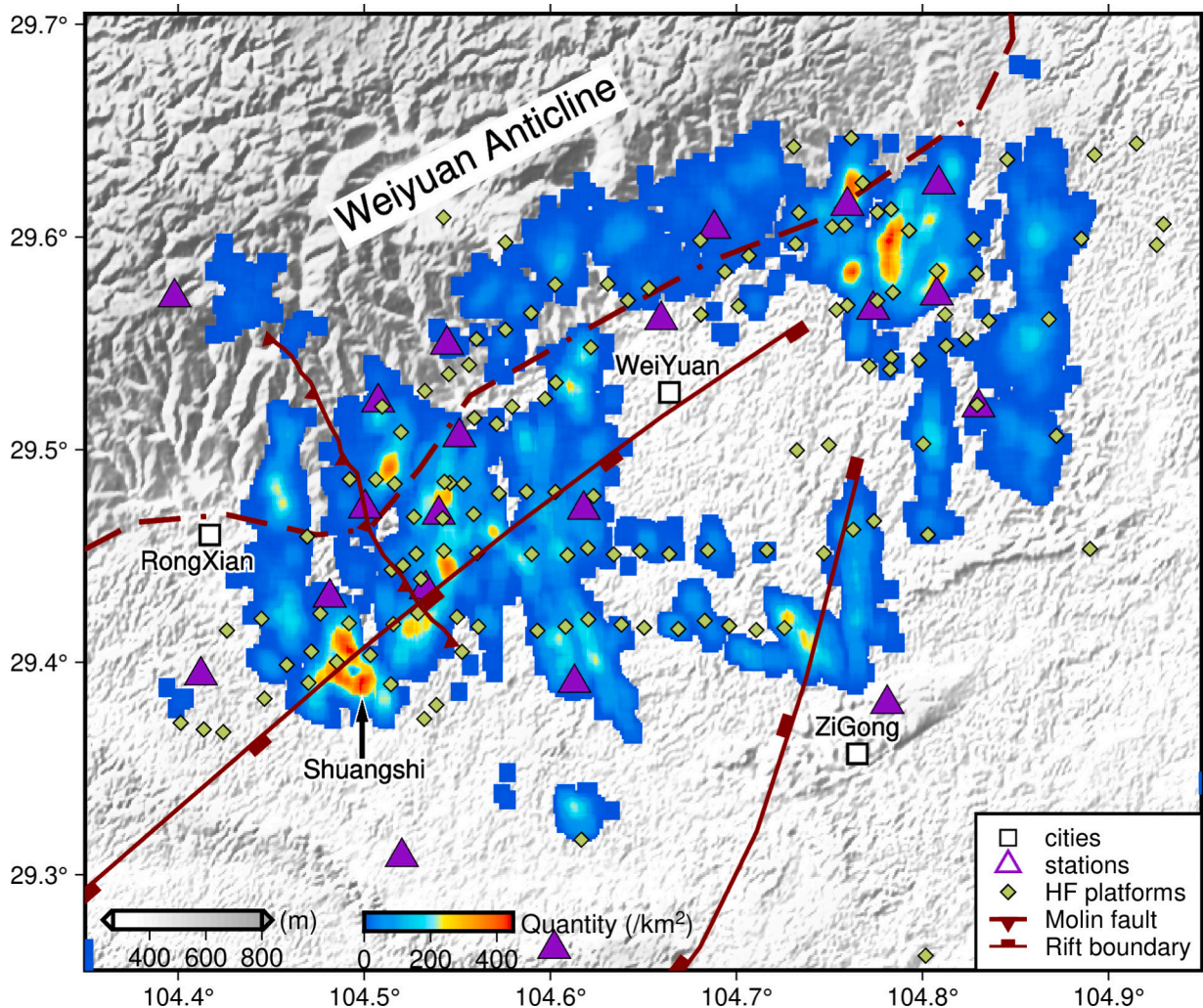


Fig. 6. Density map of relocated earthquakes. Earthquakes are separated in grids with a size of $0.001^\circ \times 0.001^\circ$ and then smoothed by convolving a 9×9 average matrix. The two largest high seismogenic-rate zones are located in the Shuangshi town and northeast Weiyuan. The red dashed line marks the boundary of the Weiyuan anticline on the surface. (For interpretation of the references to colour in this figure legend, the reader is referred to the web version of this article.)

which are located in the northwest basement rift boundary trace and to its northeast, respectively (Fig. 6). There are also some small regions with high earthquake density, indicating the existence of localized structures with intense fractures.

5.2. Velocity models

Our results show an overall down-increasing V_p and V_s pattern (Table 4), which is consistent with velocity models from Zhou et al. (2021) and Du et al. (2021). There are prominent lateral variations of the inverted V_p , V_s and corresponding V_p/V_s at different depths (Fig. 7, Fig. S7), showing variations of material features including density, shear and bulk modulus, porosity, fracture aspect ratio, and fluid content.

In this part, we select the results at depths 2 km, 4 km, and 6 km as representatives to present horizontal velocity and earthquake distribution features (Fig. 7; Fig. S7). Four cross-sections are drawn to show vertical characteristics (Fig. 5b; Fig. 8; Fig. 9). Areas with low restoration rates are masked and interpretations of key velocity features are provided.

5.2.1. Horizontal velocity structures

At the depth of 2 km, there is a low- V_p zone along the middle and southeastern Molin fault (Fig. 7a). V_s along the Molin fault present segmented features with smaller values in the northwest and southeast end (Fig. 7b). Such V_p and V_s features lead to a low V_p/V_s zone in the middle of the Molin fault (Fig. 7c). Earthquakes in the depth range of 1–3 km are projected on this map view. Seismicity is mainly located in northeast Weiyuan and the area that is close to the Molin fault. $M_L \geq 3.0$ earthquakes in northeast Weiyuan are located on the edges of high- V_p or high- V_s zones and are located at the edges of the low- V_p zone along the Molin fault (Fig. 7a, b). Few $M_L \geq 3.0$ events occur in high- V_p or high- V_s zones.

At 4 km depth, the velocity pattern that is shown at 2 km in the Molin area continues with a smaller contrast. There is a low- V_s stripe along the northwest basement rift boundary (Fig. 7e). Inside the basement rift, there exists a low- V_s zone that extends toward the northeast (Fig. 7e). Earthquakes in the depth range of 3–5 km are projected onto this depth section. Earthquakes with $M_L < 3.0$ appear to not correlate with velocity variations; rather they are well clustered near fracking platforms. In contrast, events with $M_L \geq 3.0$ are mainly located in low-velocity areas or velocity transition zones (Fig. 7d, e).

At the depth of 6 km, there is a distinct low- V_p , and low- V_s zone that extends from the rift to the northeast area (Fig. 7g, h, i), such a velocity pattern might be due to the porosity-rich sediments inside the rift. Earthquakes in the depth range of 5–8 km are projected and it also reveals that most $M_L \geq 3.0$ events are located in low-velocity or velocity transition zones inside the rift.

The September 2019 M_w 5.0 event, which is the largest earthquake by far in the WSGF, is located in the northeastern end of the velocity anomaly zone extending from the basement rift with low- V_p/V_s (Fig. 7g, h, i). Such a velocity pattern could be explained by the existence of large aspect ratio fractures (Shearer, 1988).

The correlation between earthquakes and tomographic results shows that a large number of $M_L \geq 3.0$ events locate in low-velocity zones or velocity transition zones. However, $M_L < 3.0$ clusters present distinct features; they are dominated by HF platforms locations (Fig. 5a; Fig. 7).

Our tomography results are well consistent with previous studies in the WSGF. The low- V_p velocity zone in the Molin fault area at the depth

of 2 km (Fig. 7a) and the low- V_p and - V_s zone in the basement rift at the depth of 6 km (Fig. 7g, h) are also shown in Du et al. (2021)'s tomographic results. Inside the Weiyuan anticline, the larger V_s values (Fig. 7e, h) are consistent with patterns revealed by other tomographic studies (e.g., Zeng et al., 2020; Du et al., 2021; Wei et al., 2022). Indeed, this is also consistent with the geological setting that the basement depth is shallower in the Weiyuan anticline (Gu and Wang, 2014; Wang et al., 2020).

5.2.2. Vertical velocity features

To further investigate velocity features of key structures in the WSGF, including the Molin fault that held the deadly February 2019 M_w 4.3 event (Table 1), the basement rift, and the northeast Weiyuan area that nucleated the largest M_w 5.0, we extract four vertical cross sections and compare the velocity features with HF platforms, earthquakes within two kilometers and the buried depths of the target Silurian Longmaxi formation. The map traces of four sections are shown in Fig. 5b. The section AA' and BB' extend transverse and parallel the Molin fault, respectively. Section CC' crosses the basement rift and section DD' transverses the northeast-striking $M_L \geq 3.0$ earthquake clusters in northeastern Weiyuan, which include the largest M_w 5.0 earthquake.

Along section AA', there is a low- V_p , low- V_p/V_s zone right below the Molin fault (Fig. 8); this low-velocity feature is not prominent in V_s results. Such velocity features could be explained by the existence of fractures with a large aspect ratio (e.g., 0.1; Shearer, 1988). The depth range of this low-velocity zone is ~0.5–4.0 km (Fig. 8c, g). It is distinct that earthquakes are concentrated in regions with distances from the Molin fault; seismicity beneath the Molin fault is limited. However, there are a certain number of earthquakes at depths <2 km surrounding the fault. In comparison, most earthquakes are centered at the fracking depth (Fig. 8). $M_L \geq 3.0$ events are located in the earthquake cluster to the east of the Molin fault (Fig. 5b; Fig. 8c).

Along section BB', two characterized segments are identified according to earthquake distribution and velocity features. Segment 2 has lower V_s values than segment 1 and thus leads to higher V_p/V_s (Fig. 8f, h). The low- V_s and low- V_p/V_s patterns exist in the depth range of ~1–5.5 km. $M_L \geq 3.0$ events present a stark contrast inside and outside the Weiyuan anticline. Inside the anticline the quantity of $M_L \geq 3.0$ events is small, but their magnitudes are no less than M_L 4.0. Outside the anticline, however, the number of $M_L \geq 3.0$ earthquakes is much larger but none of their magnitudes exceeds M_L 4.0. Concerning earthquake distribution, seismicity in Segment 1 dips toward NW while earthquake clusters in segment 2 dip toward SE.

The featured velocity zone of the Molin fault extends to ~4 km (Fig. 8c, g), which shows the extending depth of this fault zone. This explanation is consistent with the observation that most earthquakes occurred above 4 km along the Molin fault (Fig. 8d, f, h). In addition, the deep-penetrating earthquakes and enhanced low- V_s velocity of segment 2 in section BB', the low- V_s strip and accompanied $M_L \geq 3.0$ events lineation along the northwest basement rift boundary shown at the depth of 4 km (Fig. 7e) indicate that segment 2 of the Molin fault area received additional structural deformation from the basement rift. The low-velocity pattern in segment 2 is more prominent in V_s than V_p (Fig. 8d, f), showing there might be fluid in the cracks that can lead to a more prominent decrease in V_s (Kuster and Toksöz, 1974; Takei, 2002).

Section CC' (Fig. 9), which crosses the basement rift, shows a bow-shaped Silurian Longmaxi formation distribution. What accompanies the strata pattern are bow-shaped low- V_s and low- V_p/V_s structures. Earthquakes occurred below the target shale layer and $M_L \geq 3.0$ events only occurred inside the anticline (Fig. 9c). Section DD' presents a low- V_p and low- V_s zone in the source region of the M_w 5.0 event. This low-velocity pattern is more prominent in the depth range below 4 km (Fig. 9d, f). A large quantity of $M_L < 3.0$ events occurred above the fracking depth. $M_L > 3.0$ events not only occur inside the anticline but also in the basin area and present an increasing depth along the strike of

Table 4
Velocity value ranges at the depth of 2 km, 4 km and 6 km.

Depth (km)	V_p velocity (km/s)	V_s velocity (km/s)
2	4.80–5.56	2.83–3.15
4	5.24–6.01	3.04–3.37
6	5.15–6.04	3.23–3.61

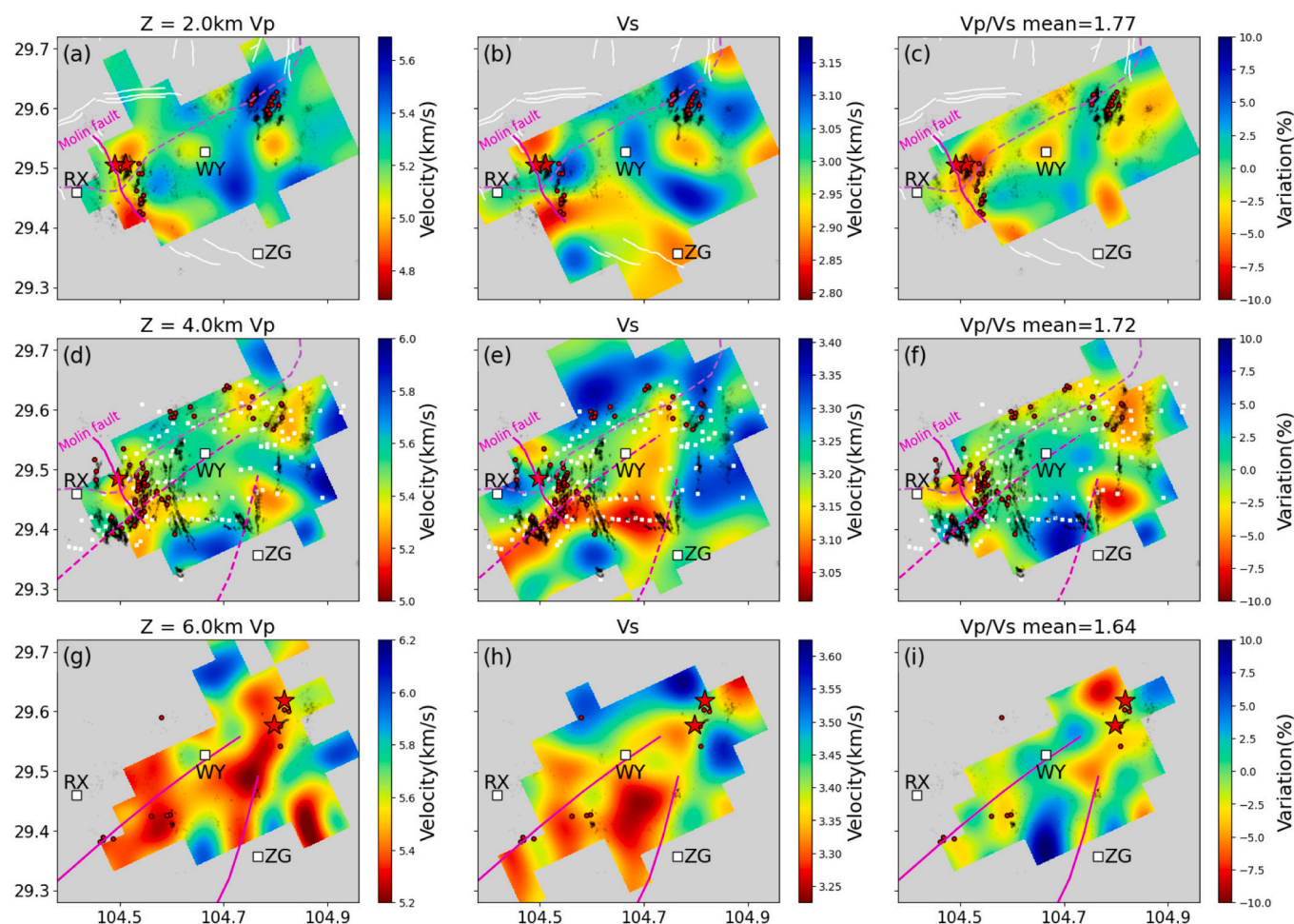


Fig. 7. Inversion results of layered V_p , V_s and V_p/V_s at 2, 4 and 6 km with faults, identified structures, and relocated earthquakes plotted. $M_L < 3.0$, $M_L 3.0-4.0$, and $M_L \geq 4.0$ events are presented by black dots, red dots and red stars, respectively. HF platforms (white squares) are projected onto the closest depth (4 km). RX: Rongxian county; ZG: Zigong city; WY: Weiyuan county. (For interpretation of the references to colour in this figure legend, the reader is referred to the web version of this article.)

section DD'.

6. Discussion

6.1. Structural constraints on earthquakes in the WSGF

$M_L \geq 4.0$ events can exert damage to facilities and $M_L \geq 3.0$ earthquakes could be sensed by residents thus leading to possible social panic. Therefore, understanding the distribution features of $M_L \geq 3.0$ events and corresponding controlling factors are critical for earthquake hazard mitigation. In this part, we will discuss the structural constraints from the Weiyuan anticline, the basement rift, and revealed tomographic features.

6.1.1. Structural constraints from the Weiyuan anticline

The Weiyuan anticline is a wedge structure controlled by a deep northwest-dipping thrust ramp and a shallow southeast-dipping back-thrust detachment fault rooted in Cambrian at ~ 5 km (Hubbard and Shaw, 2009; Wang et al., 2020; Jia et al., 2020). Kinematic simulation of detachment thrust-faulting shows that besides the strain in the front of the thrust fault tip, the backlimb of the fold also experienced strong deformation (Fig. 10). The backlimb trishear (Cristallini and Allmendinger, 2002) area, which centers the active axial surface, accommodates strain from the deformed backlimb to the flat weak strain area. Therefore, the region could be separated into three segments that

experienced strong, moderate, and weak structural deformation (Fig. 10; Fig. S8; Table S3).

For the domain with a depth of <5 km in the WSGF, which is the structural deformation domain of the Weiyuan anticline, there are two distribution features of $M_L \geq 3.0$ events. The first one is that all $M_L \geq 4.0$ occurred inside the Weiyuan anticline, including the two in this study period, and the other four for the period from mid-2015 to February 2019 (Fig. 5c). No $M_L \geq 4.0$ events occurred in the basin area even though the quantity of $M_L \geq 3.0$ events is large. The second feature is that $M_L \geq 3.0$ events are concentrated in or close to the Weiyuan anticline. Seismicity clusters far from the Weiyuan anticline are accompanied by no $M_L \geq 3.0$ events. The two features are well correlated with the structural deformation simulation of the Weiyuan anticline. The area experiencing strong tectonic deformation can generate larger fractures that could hold greater earthquakes, which is consistent with the observation that $M_L \geq 4.0$ events only occurred in the anticline backlimb (Fig. 5c). The intense occurrence of $4.0 > M_L \geq 3.0$ in close areas along the anticline edges and no $M_L \geq 3.0$ events in the areas far from the anticline also comply with the strain difference between moderate and weak strain zones.

The most recent structural deformation of the Weiyuan anticline started in 30.8 Ma (Richardson et al., 2008) in response to the Himalayan movement. Southeast decreasing GPS velocities show the basin still under tectonic loading (Fig. 1a). Since the 1600s, 14 natural earthquakes with magnitude >5 occurred inside the Sichuan Basin,

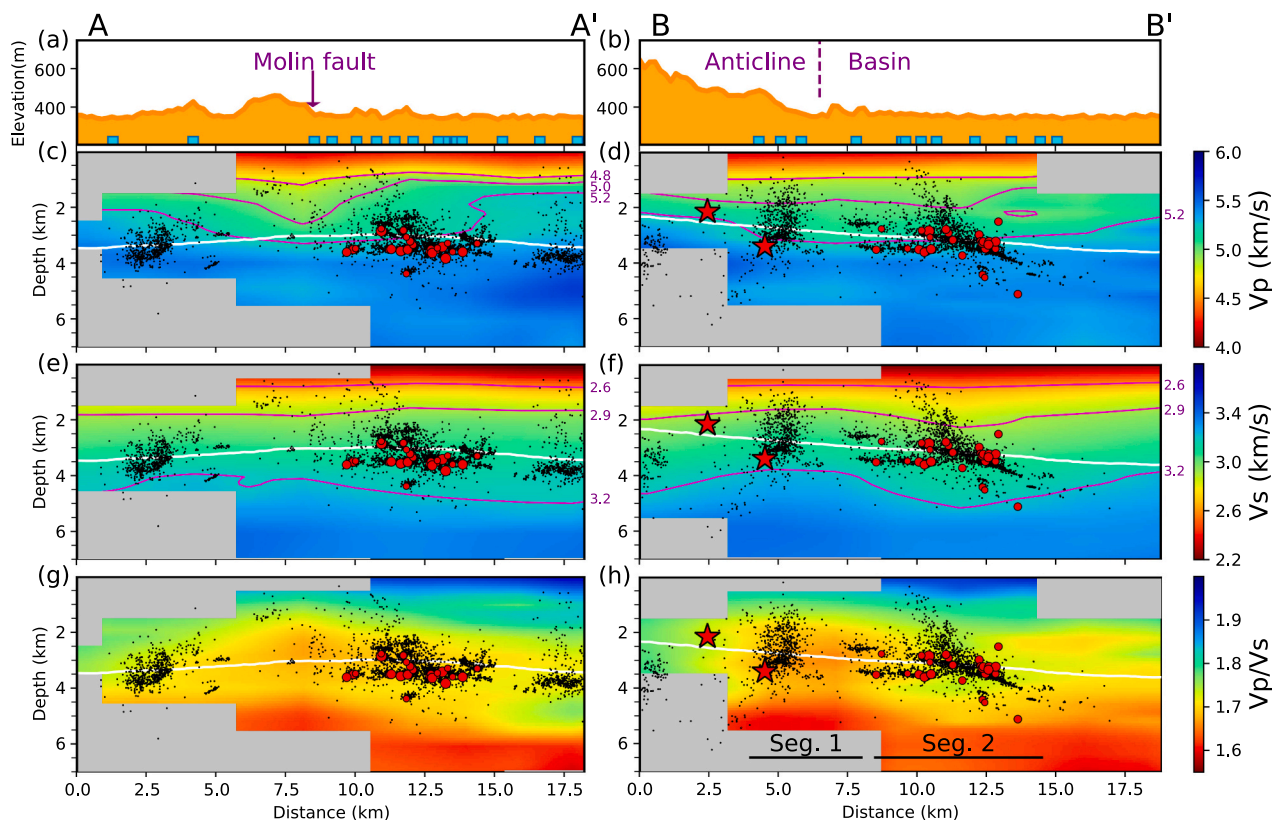


Fig. 8. V_p (c, d), V_s (e, f), and V_p/V_s (g, h) results along section AA' and BB' with topography (a, b), HF platforms within 2 km (cyan squares in a, b), earthquakes within 2 km, and the target shale layer (white lines) plotted. Cross-section traces are plotted in Fig. 5. $M_L < 3.0$, $M_L 3.0-4.0$, and $M_L \geq 4.0$ events are presented by black dots, red dots, and red circles, respectively. (For interpretation of the references to colour in this figure legend, the reader is referred to the web version of this article.)

including the M5.0 in Weiyuan (Lei et al., 2020). Therefore, it is highly likely that some well-oriented faults are in critical condition under the current east-west SH_{max} direction. The intense occurrence of $M_L \geq 4.0$ in northeast Weiyuan and in the Molin area further favors this inference (Fig. 5b). Therefore, we conclude that the structural deformation of the Weiyuan anticline controls the magnitude and location of $M_L \geq 3.0$ events for the domain < 5.0 km in the WSGF by the generated fracture sizes and loaded tectonic stress.

6.1.2. Structural constraints from the basement rift

For the domain with a depth > 5.0 km, the basement rift is the dominant structure. Most $M_L \geq 3.0$ earthquakes with depths > 5.0 km are located within or to the northeast of the basement rift zone (Fig. 5d). The basement rift boundaries, which are identified from seismic reflection profiles (Hu et al., 2022), didn't extend to the northeast-striking $M_L \geq 3.0$ cluster in northeastern Weiyuan. However, tomography results show that a low- V_p and low- V_s zone connects the rift zone and the northeastern Weiyuan $M_L \geq 3.0$ event cluster (Fig. 7 g,h,i). Given the depth and strike consistency between the northeast $M_L \geq 3.0$ cluster and the basement rift, and the tomography velocity anomaly connection, we speculate that the basement rift zone extends to the northeast area where the northeast $M_L \geq 3.0$ event cluster is located. The width of the basement rift becomes narrower toward the northeast, which is consistent with the width variation of the deep low- V_s zone in section CC' and DD' (Fig. 9).

There have been reported cases that some Neoproterozoic basement rift faults extend to shallower depths (Hu et al., 2022; Gu and Wang, 2014). Such an inherited propagation might be due to extensional settings in later geological stages. E.g., in late-Cambrian and in late-Permian (Liu et al., 2021). Some studies also infer that the

reactivation of basement faults in the Late Cambrian is the structural reason for the formation of the Weiyuan-Anyue giant gas reservoir to the north of the WSGF (Li et al., 2015; Zi et al., 2017). In the WSGF, bow-shaped strata deformation across the basement rift (Fig. 9f; Figure 7 in Jia et al., 2020) and features along the northwest basement rift trace including the low- V_s strip, the $M_L \geq 3.0$ lineation (Fig. 7e, Fig. 5c), and the high seismicogenic rate (Fig. 6) evident inherited deformation of the basement rift in later geological stages. Thus, it is likely that some faults inside the rift zone propagate upward in later structural deformation and generate a large number of fractures. These faults and fractures have the capabilities to be reactivated under the contractional setting of the basin since the late Triassic. In addition, most HF-related earthquakes occurred within 2 km from the injection site horizontally and are more confined in depth (Atkinson et al., 2020). However, seismicity diffusion distance could be boosted with the existence of faults as conduits, e.g., in the WSGF (Sheng et al., 2022) and Alberta, Canada (Schultz et al., 2015). The occurrence of a number of events below 5 km (Fig. 5d; Fig. 7 g, h, i) favors the existence of fractures/faults as conduits to build connections between injection sites and deep earthquake nucleation locations. Thus, we infer that the structural deformation of the basement rift in the WSGF is the dominant structure that influences the location of $M_L \geq 3.0$ events in the deep domain.

6.1.3. Lateral variations along the anticline strike

For the domain with a depth of < 5 km, in addition to earthquake magnitude and location variations from the Weiyuan anticline to its southeastern basin region. Changes also exist along the strike toward northeast. It is shown that $M_L \geq 4.0$ events are mainly concentrated in the Molin area, close to the Molin fault zone which has an extending depth of ~ 4 km as revealed by our tomography results. However, Wang

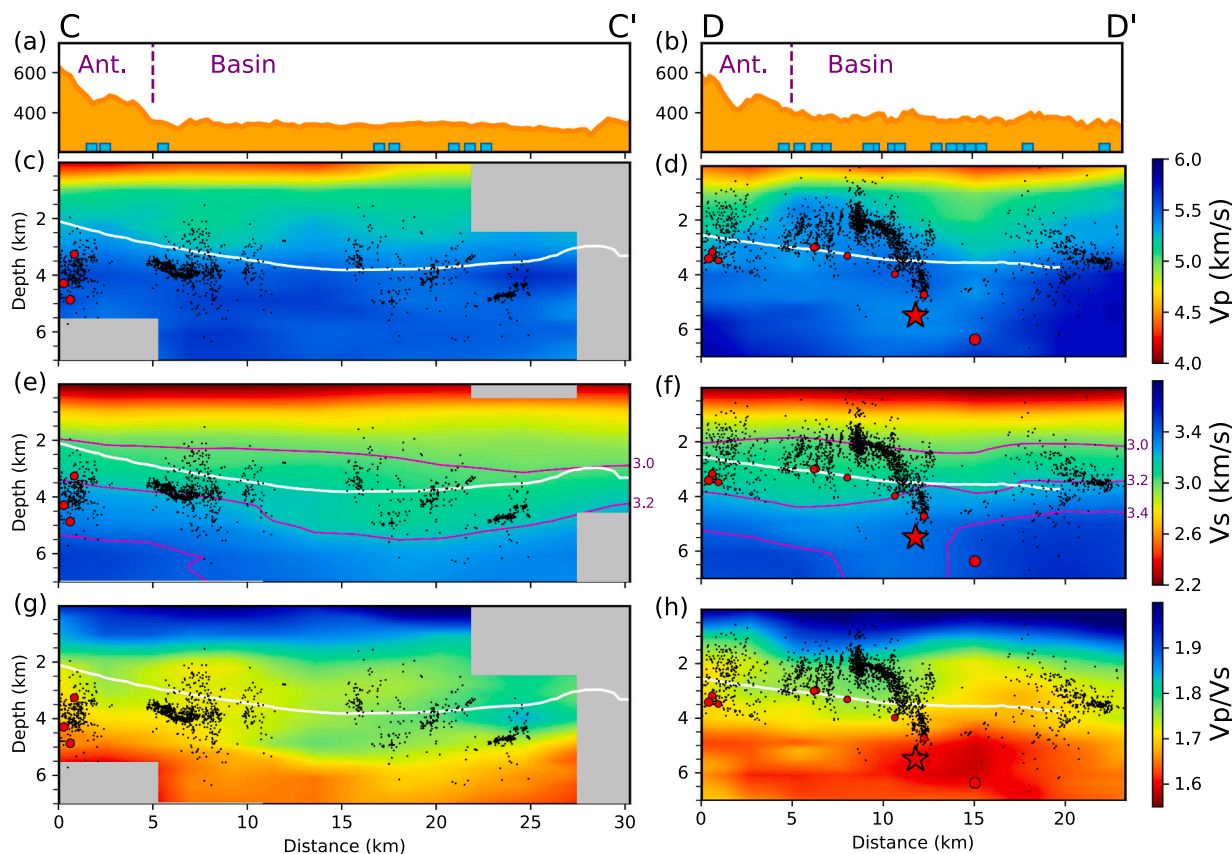


Fig. 9. Same with Fig. 8 except section traces. (For interpretation of the references to colour in this figure legend, the reader is referred to the web version of this article.)

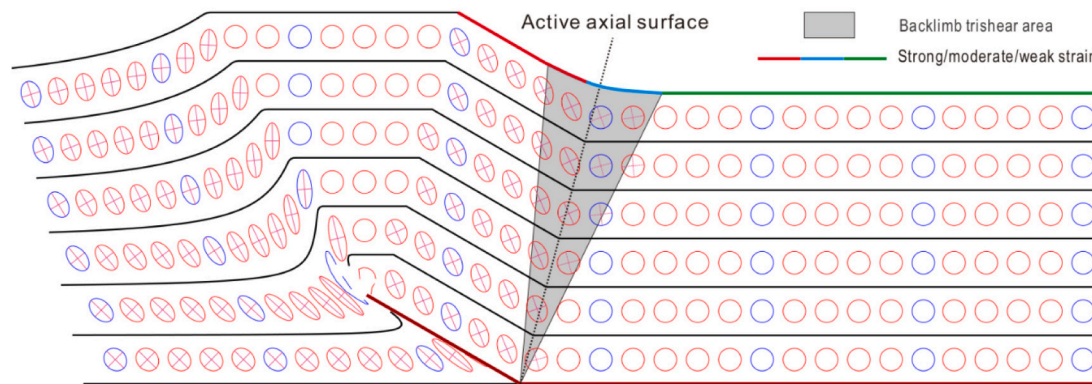


Fig. 10. Adjusted numerical simulation results of detachment thrust-faulting with strain ellipses and principal axes shown. Inside the fold, strong strain is accumulated during structural deformation. The area in the vicinity of the active axis receives moderate strain. While regions distant from the anticline gain weak/no strain.

et al. (2020) identified the Molin fault, which is a tear fault and nucleated the deadly February 2019 M_w 4.3 event (Yang et al., 2020), as a shallow fault that extends no deeper than 1.5 km based on the interpretation of a 2-D seismic reflection profile. Therefore, we infer that there are blind faults in the Molin fault zone that extend to ~ 4 km and the Molin fault is the most prominent one that ruptured the surface. This inference is further favored by the occurrence of other $M_L \geq 4.0$ events in the Molin area that are not on the Molin fault trace (Fig. 1b; Fig. 5c).

The existence of tear faults, which accommodate changes of thrust fault segments on its two sides (Benesh et al., 2014), indicates contrast in the thrust fault plane or slip pattern along the strike, which can further

promote the occurrence of fractures that could be activated under current east-west compressional tectonic stress field (Chen et al., 2018) in addition to the thrust-faulting structural deformation. Despite magnitudes differences along the strike, the controlling effects from the Weiyuan anticline on earthquake locations and magnitudes remain prominent (Fig. 5b; section BB' in Fig. 8; section CC' in Fig. 9) except for northeast Weiyuan, where a larger quantity of $M_L \geq 3.0$ events occur in the basin area (Fig. 5c). We infer the enhanced capability of occurring $M_L \geq 3.0$ events in northeast Weiyuan is due to additional structural deformation from the basement rift.

6.1.4. Structural constraints revealed by tomographic results

Tomographic results show that a large number of $M_L \geq 3.0$ events are located in low- V_p /low- V_s velocity zones or velocity transition zones and rarely occurred in high- V_p /high- V_s zones (Fig. 7). We infer the correlation between $M_L \geq 3.0$ events and low-velocity zones is due to intense fractures in low-velocity zones that could hold $M_L \geq 3.0$. The horizontal velocity transition zones might mark the boundary of localized structures and thus have unstable stress conditions. Similar tomographic results are revealed in other areas. For example, Tan et al. (2019) and He et al. (2021) conducted tomography studies in the Changning shale gas field, Sichuan, and one wastewater disposal field in Oklahoma, respectively. Their results also favor that earthquakes are more prone to occur in fracture-rich areas.

In summary, our results show that the Weiyuan anticline and the basement rift are the two key structures in the WSGF that exert constraints on the locations and magnitudes of $M_L \geq 3.0$ events and lead to contrasting depths of $M_w \geq 4.0$ events in northeast Weiyuan and the Molin area (Table 1). They constrain the maximum magnitudes by influencing the fracture sizes. Such constraints present along-strike variations. More specific locations are correlated with subsurface structure characteristics, such as fracture densities and localized structures that could be revealed in tomography results.

6.2. The fault plane of the September 2019 M_w 5.0 event

The September 2019 M_w 5.0 event is by far the largest HF-triggered earthquake in the WSGF which leads to 1 death and 63 injuries. Understanding the triggering mechanism of such a destructive event is therefore critical for earthquake hazard mitigation. Focal mechanism results reveal that this event is a reverse-faulting earthquake (Fig. 11; Table 1). However, there are still debates on the source parameters, including the rupture plane and the centroid depth, which inhibited our understanding of the potential triggering mechanism of this earthquake (Table 1).

The distribution of aftershocks due to the static stress transfer of the main shock has been widely used to constrain the fault plane (e.g., Yang et al., 2009). Aftershocks of the M_w 5.0 event present NE-SW distribution (Fig. 11a). We use 815 aftershocks that occurred within 14 days after the M_w 5.0 (Fig. 11c) to conduct the least square fault-plane fitting, and we get the best-fit strike and dip angle values at 30.3° and 42.6° , respectively (text S1). The rupture area of a M_w 5.0 event is estimated to be $\sim 10 \text{ km}^2$ (Wells and Coppersmith, 1994), corresponding to a radius of 1.8 km by assuming a circular plane. Combining the fault plane parameters, the rupture area should be below 3.1 km. Therefore, our result is consistent with centroid depths reported by Wang et al. (2020) and Yi et al. (2020) (Table 1). Combining our earthquake relocation results, tomography interpretation, aftershocks lineation, and previously

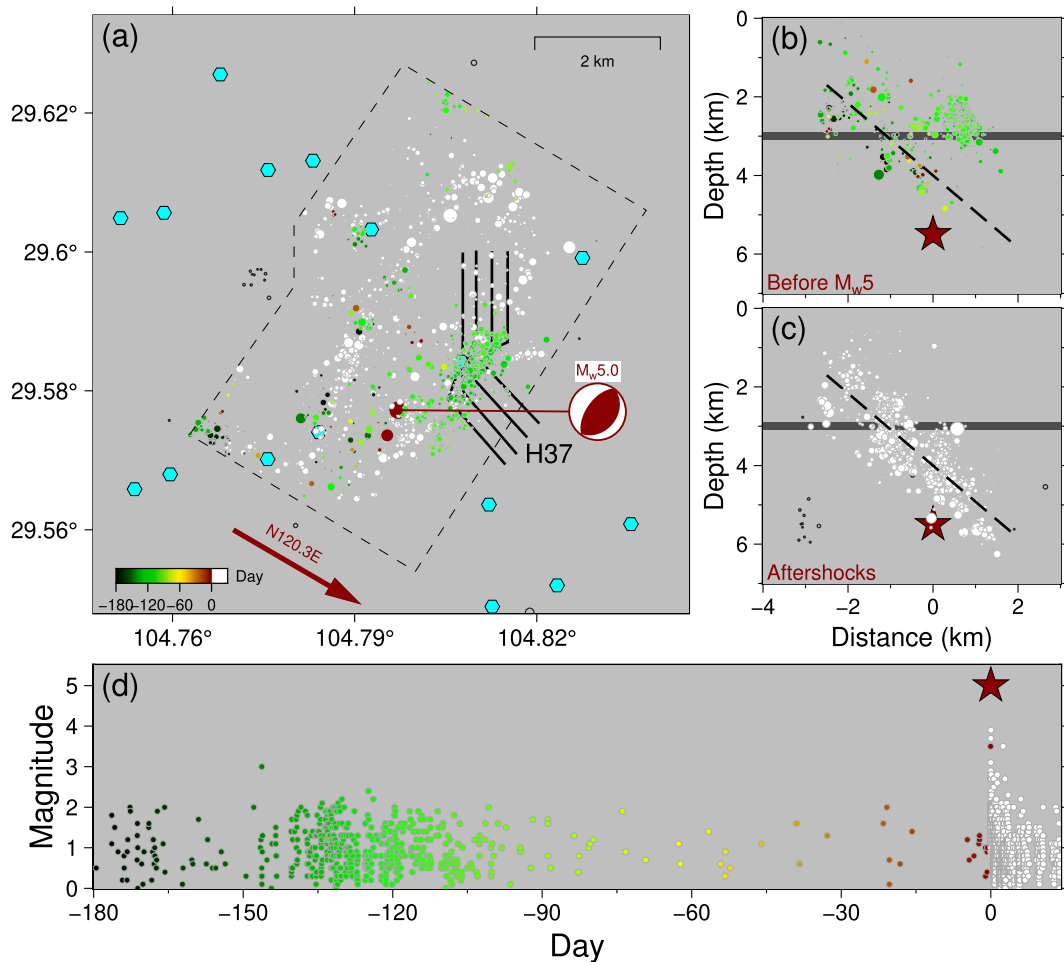


Fig. 11. Distribution of earthquakes in the vicinity of the M_w 5.0. (a) Map view of earthquakes that occurred before (colored) and after (white) the M_w 5.0. Platform H37 experienced fracking before the M_w 5.0. Aftershocks inside the dashed polygon are used to estimate the fault plane parameters. Earthquakes in dark grey are not included in fault plane estimation due to their inconsistent locations and depths. The red arrow denotes the dip azimuth. (b) Projection of earthquake before the M_w 5.0 along the dip direction. The dashed black line denotes the best-fit fault trace constrained by aftershocks. (c) Projection of aftershocks along the dip direction with the best-fitting fault plane shown. (d) Magnitude versus time plot of earthquakes in the vicinity of the M_w 5.0. The H37 fracking seismicity occurred 3–5 months before the mainshock. (For interpretation of the references to colour in this figure legend, the reader is referred to the web version of this article.)

reported centroid depths, we conclude that the M_w 5.0 nucleated in a northeast-striking fault plane located in a deep geological susceptibility zone that influenced by the basement rift with a dip angle of 42.6° at 5.5 km. The rupture propagated upward with a centroid depth in ~ 4.5 –5 km.

Several studies have attempted to address the triggering mechanism of this event (e.g., Wang et al., 2020; Lei et al., 2020; Sheng et al., 2020). Nevertheless, different results lead to biased explanations. Our results show that the M_w 5.0 nucleated at a depth of 5.5 km, which is a depth closer to the fracking depth in comparison to hypocenters reported in other studies (e.g., Du et al., 2021). There is a cluster of earthquakes that occurred on the H37 platform several months before the mainshock, which we infer is due to the fracking activity (Fig. 11). Accordingly, some seismicity seems to occur on the fault plane well before the mainshock, indicating a potential fluid diffusion process (Fig. 11b). However, whether fluids have migrated into the fault and triggered the M_w 5.0 needs to be resolved with an enhanced catalog (e.g., template matching), as well as a reliable geomechanical model, which are not available right now.

6.3. Implications for seismic hazard mitigation

Although there is a common consensus that geological settings are correlated with moderate earthquakes in shale gas fields (Schultz et al., 2020; Atkinson et al., 2020; Lei et al., 2020; Kao et al., 2018), a series of questions remain unclear, including to what extent geological settings influence locations and magnitudes of earthquakes and whether geological susceptibility zones could be identified. Thus, research addressing these questions could promote our understanding of HF-related earthquakes.

The total injection volume is an important factor in estimating the potential maximum induced earthquake magnitude (McGarr, 2014). The fault patch size is another principal factor that constrains the upper bound of earthquake magnitudes. In the WSGF, constraints of magnitudes from the Weiyuan anticline structural deformation are prominent as evidenced by earthquake magnitudes contrast in different tectonic strain zones. Therefore, additional caution should be paid when fracking was conducted in the Weiyuan anticline backlimb and along the basement rift boundary zones.

Similar patterns are also shown in the Western Canada Sedimentary Basin (Kao et al., 2018). Moderate earthquakes are concentrated in the foothills of mountains that received structural deformation, and earthquake quantity and magnitudes inside the basin area are small. Thus, identifying high tectonic strain areas which might contain large fractures would be critical for earthquake hazard mitigation in structural deformation complex regions, for example, the Changning and Luzhou shale gas fields (Fig. 1a). Structural kinematic simulation and tomography could be applied to reveal detailed high-strain areas and fracture-rich regions.

Besides seismicity clusters that transverse the strata distribution, some clusters occurred offset the fracking depth and distributed parallel to strata (section BB' in Fig. 8, section CC' in Fig. 9). These earthquakes might occur on detachment faults. Detachment faults developed in Triassic and Cambrian strata have distinct impacts on structural deformation in the Sichuan Basin (Jia et al., 2020; Wang et al., 2020). For example, the fault slip of the eastern Sichuan fold belt is interpreted to be accommodated by detachment faults rooted in Cambrian strata. Detachment faults have the capability to start earthquakes on high-angle thrust faults that are difficult to reactivate. By far, magnitudes of seismicity on potential detachment faults are small (e.g., Section CC') and there have been no reported cases that correlate detachment faults with moderate induced earthquakes in the Sichuan Basin. However, the seismic hazard potential exerted by detachment faults activation shouldn't be ignored. Our study reveals how the structural controlling effect on $M_L \geq 3.0$ earthquakes is achieved for HF-related earthquakes and might be the first report that reveals impacts on HF-related

earthquakes from the basement rift in the Sichuan Basin. With the planning of massive HF in deeper shale layers (e.g., Qiongzhusi formation in Cambrian) in the Sichuan Basin, the impacts on earthquake distribution from basement structures would be more prominent. Thus, earthquake hazard assessment including a thorough study of basement structures would be critical.

6.4. Limitations

Benefiting from the combination of the SEA network and the temporary network, our study reveals detailed velocity structures in the WSGF. High-resolution earthquake relocation is conducted using the inverted 3D velocity models. However, one limitation of this study lies in the limited information that could be provided for HF safety operations. Our tomography models are in a horizontal resolution of $0.05^\circ \times 0.05^\circ$ (~ 4.8 km along the longitude and ~ 5.5 km along the latitude) in focused areas. Such setup can reveal dominant structures in the WSGF but is too large in view of lengths of horizontal wells that are in the range of ~ 1 –2 km, thus leading to limited capability to reveal susceptible structures that could provide critical insights for hazard mitigation during HF operation. In recent years, the development of dense array studies has promoted our understanding of subsurface structures through high-resolution tomography. Deployment of dense array networks in shale gas fields would be a plausible method to provide fine structure information for hazard mitigation references.

A second limitation lies in limited information about faults related to the basement rift. Even though Hu et al. (2022) reported the location of the basement rift in WSGF, less is published related to fault features in the rift structure, which inhibits our further understanding. For example, our tomography results show that the basement rift extends further to the northeast with smaller velocity contrasts (Fig. 7g, h), which is consistent with weak strata deformation in section DD' (Fig. 9d), showing relatively smaller tectonic strain accumulation in the northeast. However, it has been observed that by far, the largest two events only occurred in the northeast. The Shuangshi area, which is another high earthquake productivity zone as the northeastern Weiyuan (Fig. 6), is obsessed with no $M_L \geq 4.0$ events occurrence. A possible scenario is that the limited rifting effect in the northeast of the basement rift leads to gentle fault planes that are more prone to reactivate under current contractional geological settings. Nevertheless, we are not able to verify the scenario until further information concerning the basement rift faults is revealed. Furthermore, the occurrence of an earthquake is a complicated process involving a variety of factors including fault plane stress conditions, stress perturbations, and frictional properties. It has been shown that earthquakes nucleated in different areas of a fault plane could lead to distinct moment releases (Yang et al., 2019; Yao and Yang, 2022). Thus, the occurrence of the M_w 5.0 and the M_w 4.9 event in northeast Weiyuan rather than other areas influenced by the structural deformation of the basement rift might be due to the earthquake nucleation process. The determination of the fault plane of the September 2019 M_w 5.0 is the first step toward the revealing of the triggering process. Further geomechanical simulation investigation can be conducted to reveal the scenario from injection to the nucleation of this damaging event, which is significant in earthquake hazard mitigation.

7. Conclusion

We conducted body-wave tomography inversion, earthquake relocation, and structural analysis in the WSGF, Sichuan Basin, China. Our results show that it is the structural deformation of the Weiyuan anticline and the basement rift that controls the location and magnitude of $M_L \geq 3.0$ events in the WSGF. Details are:

- In the structural influential domain of the Weiyuan anticline (depth < 5 km), fractures and tectonic strain loading during the anticline

structural deformation lead to decreased maximum earthquake magnitudes from the anticline to the basin area. Inside the anticline, the large fracture sizes and high tectonic strain loading allow for the occurrence of a number of $M_L \geq 4.0$ events. In the anticline-basin transition zone, the limited fracture sizes constrain earthquake magnitudes within $M_L 4.0$. Further to the basin area, more confined fracture sizes lead to no observation of $M_L \geq 3.0$ earthquakes.

- The structural deformation of the basement rift constrains locations of deep (depth ≥ 5 km) $M_L \geq 3.0$ earthquakes located within the rift zone, leads to shallow $M_L \geq 3.0$ (depth < 5 km) lineations and enhances earthquake productivity along the basement rift trace.

Our study in the WSGF provides a clear relationship illustrating how structural deformation within a shale gas field influence earthquake locations and magnitudes. The revealing of impacts on earthquakes from the newly reported basement rift provides valuable information for earthquake hazard mitigation. Besides, $M_L \geq 3.0$ events are found to be more prone to occur in low-velocity zones and velocity transition zones that are geologically unstable. Therefore, structural deformation simulation and tomography study could be useful tools to identify geologically susceptible areas in shale gas fields.

We further use aftershocks to refine the fault plane of the largest HF-triggered earthquake, the September 2019 M_w 5.0 event, in the WSGF. Aftershocks delineate a southeast-dipping fault plane with a strike and a dip angle at $N30.7^\circ E$ and 43.2° , respectively. Combining the tomography results, we infer that the M_w 5.0 event nucleated in a northeast-striking fault that is influenced by the structural deformation of the basement rift.

CRediT authorship contribution statement

Jinping Zi: Formal analysis, Investigation, Methodology, Visualization, Conceptualization, Writing - original draft, Writing - review & editing. **Hongfeng Yang:** Conceptualization, Funding acquisition, Investigation, Project administration, Supervision, Writing - review & editing. **Jinrong Su:** Data curation, Investigation. **Liang Chen:** Investigation, Resources.

Declaration of Competing Interest

We declare that we have no financial and personal relationships with other people or organizations that can inappropriately influence our work, and there is no professional or other personal interest of any nature or kind in any product, service and/or company that could be construed as influencing the position presented in, or the review of, the manuscript entitled.

Data availability statement

The inversion inputs, the output catalog and velocity models, and the HF platform locations are

available in Zenodo (<https://doi.org/10.5281/zenodo.7997520>). Event waveforms of the temporary catalog can be downloaded at <https://doi.org/10.17632/bp7dzg82p6>. Figures are prepared using GMT (Wessel et al., 2019) and Python. Magnitude completeness (M_c) and b values are calculated using the ZMAP software (Wiemer, 2001). Thrust-faulting kinematic simulation is conducted using the FaultFold-Forward program (Allmendinger, 1998) and modified according to the backlimb trishear theory (Cristallini and Allmendinger, 2002).

Acknowledgments

We appreciate constructive comments and suggestions from two anonymous reviewers. We thank Dr. Pengcheng Zhou and Prof. Risheng Chu's team for sharing the temporary network catalog and travel times

(Zhou et al., 2021; Sheng et al., 2022). We acknowledge Prof. Chuen Hon Arthur Cheng for the inspiring discussion. This work is supported by the National Natural Science Foundation of China (No. U2139203), Hong Kong Research Grant Council Grants (No. 14303721), Faculty of Science in The Chinese University of Hong Kong, and Hong Kong PhD Fellowship Scheme.

Appendix A. Supplementary data

Supplementary data to this article can be found online at <https://doi.org/10.1016/j.tecto.2023.230007>.

References

- Allmendinger, R.W., 1998. Inverse and forward numerical modeling of trishear fault-propagation folds. *Tectonics* 17 (4), 640–656. <https://doi.org/10.1029/98TC01907>.
- Atkinson, G.M., Eaton, D.W., Igonin, N., 2020. Developments in understanding seismicity triggered by hydraulic fracturing. *Nat. Rev. Earth Environ.* 1 (5), 264–277. <https://doi.org/10.1038/s43017-020-0049-7>.
- Bao, X., Eaton, D.W., 2016. Fault activation by hydraulic fracturing in western Canada. *Science* 354, 1406–1409. <https://doi.org/10.1126/science.aag2583>.
- Benesh, N.P., Plesch, A., Shaw, J.H., 2014. Geometry, kinematics, and displacement characteristics of tear-fault systems: an example from the deep-water Niger Delta. *AAPG Bull.* 98 (3), 465–482. <https://doi.org/10.1306/06251311013>.
- Chen, H., Meng, X., Niu, F., Tang, Y., Yin, C., Wu, F., 2018. Microseismic monitoring of Stimulating Shale Gas Reservoir in SW China: 2. Spatial Clustering Controlled by the Preexisting Faults and Fractures. *J. Geophys. Res. Solid Earth* 123 (2), 1659–1672. <https://doi.org/10.1002/2017JB014491>.
- Cristallini, E.O., Allmendinger, R.W., 2002. Backlimb trishear: a kinematic model for curved folds developed over angular fault bends. *J. Struct. Geol.* 24 (2), 289–295. [https://doi.org/10.1016/s0191-8141\(01\)00063-3](https://doi.org/10.1016/s0191-8141(01)00063-3).
- Du, G., Wu, Q., Zhang, X., Zhang, R., 2021. Activity characteristics of moderate and small earthquakes and fine crustal feature beneath Weiyuan, Sichuan and adjacent areas. *Chin. J. Geophys.* 64 (11), 3983–3996. <https://doi.org/10.6038/cjg202100452> in Chinese.
- Efron, B., 1982. The Jackknife, the Bootstrap and Other Resampling Plans. *Soc. Indust. Appl. Math.* <https://doi.org/10.1137/1.9781611970319>.
- Efron, B., Tibshirani, R., 1991. Statistical data analysis in the computer age. *Science* 253 (5018), 390–395. <https://doi.org/10.1126/science.253.5018.390>.
- Ellsworth, W.L., 2013. Injection-Induced Earthquakes. *Science* 341, 1225942. <https://doi.org/10.1126/science.1225942>.
- Eyre, T.S., Eaton, D.W., Garagash, D.I., Zecevic, M., Venieri, M., Weir, R., Lawton, D.C., 2019. The role of aseismic slip in hydraulic fracturing-induced seismicity. *Sci. Adv.* 5 (8), 1–10. <https://doi.org/10.1126/sciadv.aav7172>.
- Grigoli, F., Cesca, S., Priolo, E., Rinaldi, A.P., Clinton, J.F., Stabile, T.A., et al., 2017. Current challenges in monitoring, discrimination, and management of induced seismicity related to underground industrial activities: a European perspective. *Rev. Geophys.* 55 (2), 310–340. <https://doi.org/10.1002/2016rg000542>.
- Grigoli, F., Cesca, S., Rinaldi, A.P., Manconi, A., López-Comino, J.A., Clinton, J.F., et al., 2018. The November 2017 M_w 5.5 Pohang earthquake: a possible case of induced seismicity in South Korea. *Science* 360 (6392), 1003–1006. <https://doi.org/10.1126/science.aat2010>.
- Gu, Z., Wang, Z., 2014. The discovery of Neoproterozoic extensional structures and its significance for gas exploration in the Central Sichuan Block, Sichuan Basin, South China. *Sci. China Earth Sci.* 57 (11), 2758–2768. <https://doi.org/10.1007/s11430-014-4961-x>.
- Guo, H., Zhang, H., 2017. Development of double-pair double difference earthquake location algorithm for improving earthquake locations. *Geophys. J. Int.* 208 (1), 333–348. <https://doi.org/10.1093/gji/ggw397>.
- Guo, H., Zhang, H., Froment, B., 2018. Structural control on earthquake behaviors revealed by high-resolution Vp/Vs imaging along the Gofar transform fault, East Pacific rise. *Earth Planet. Sci. Lett.* 499, 243–255. <https://doi.org/10.1016/j.epsl.2018.07.037>.
- Guo, H., McGuire, J.J., Zhang, H., 2021. Correlation of porosity variations and rheological transitions on the southern Cascadia megathrust. *Nat. Geosci.* 14 (5), 341–348. <https://doi.org/10.1038/s41561-021-00740-1>.
- He, L., Wu, Q., Chen, X., Sun, X., Guo, Z., Chen, Y.J., 2021. Detailed 3D Seismic Velocity Structure of the Prague, Oklahoma Fault Zone and the Implications for Induced Seismicity. *Geophys. Res. Lett.* 48 (24), e2021GL096137 <https://doi.org/10.1029/2021GL096137>.
- Hu, J., Jia, D., Wei, G., Xie, W., Li, Y., Su, N., et al., 2022. Seismic reflection analysis of the deeply buried Neoproterozoic rift basin beneath Sichuan Basin, southern China. *AAPG Bull.* <https://doi.org/10.1306/10212120127>.
- Hubbard, J., Shaw, J.H., 2009. Uplift of the Longmen Shan and Tibetan plateau, and the 2008 Wenchuan ($M = 7.9$) earthquake. *Nature* 458 (7235), 194–197. <https://doi.org/10.1038/nature07837>.
- Jia, D., Li, Y., Yan, B., Li, Z., Wang, M., Chen, Z., Zhang, Y., 2020. The Cenozoic thrusting sequence of the Longmen Shan fold-and-thrust belt, eastern margin of the Tibetan plateau: Insights from low-temperature thermochronology. *J. Asian Earth Sci.* 198, 104381 <https://doi.org/10.1016/j.jseas.2020.104381>.
- Jiang, G., Qiao, X., Wang, X., Lu, R., Liu, L., Yang, H., et al., 2020. GPS observed horizontal ground extension at the Hutubi (China) underground gas storage facility

- and its application to geomechanical modeling for induced seismicity. *Earth Planet. Sci. Lett.* 530 <https://doi.org/10.1016/j.epsl.2019.115943>.
- Kao, H., Hyndman, R., Jiang, Y., Visser, R., Smith, B., Babaie Mahani, A., et al., 2018. Induced Seismicity in Western Canada Linked to Tectonic Strain Rate: Implications for Regional Seismic Hazard. *Geophys. Res. Lett.* 45 (20), 11,104–11,115. <https://doi.org/10.1029/2018GL079288>.
- Keranan, K.M., Savage, H.M., Abers, G.A., Cochran, E.S., 2013. Potentially induced earthquakes in Oklahoma, USA: Links between wastewater injection and the 2011 Mw 5.7 earthquake sequence. *Geology* 41 (6), 699–702. <https://doi.org/10.1130/g34045.1>.
- Kim, K., Ree, J., Kim, Y., Kim, S., Kang, S.Y., Seo, W., 2018. Assessing whether the 2017 Mw 5.4 Pohang earthquake in South Korea was an induced event. *Science* 360, 1007–1009. <https://doi.org/10.1126/science.aat6081>.
- Klein, F.W., 2002. *User's Guide to HYPOINVERSE-2000, a Fortran Program to Solve for Earthquake Locations and Magnitudes*. US Geological Survey.
- Kuster, G.T., Toksöz, M.N., 1974. Velocity and attenuation of seismic waves in two-phase media: part I. Theoretical formulations. *Geophysics* 39 (5), 587–606. <https://doi.org/10.1190/1.1440450>.
- Lei, X., Wang, Z., Su, J., 2019. The December 2018 M_L 5.7 and January 2019 M_L 5.3 Earthquakes in South Sichuan Basin Induced by Shale Gas Hydraulic Fracturing. *Seismol. Res. Lett.* 90 (3), 1099–1110. <https://doi.org/10.1785/0220190029>.
- Lei, X., Su, J., Wang, Z., 2020. Growing Seismicity in the Sichuan Basin and its Association with Industrial Activities. *Sci. China Earth Sci.* <https://doi.org/10.1007/s11430-020-9646-x>.
- Li, Z., Li, X., Kinny, P., Wang, J., Zhang, S., Zhou, H., 2003. Geochronology of Neoproterozoic syn-rift magmatism in the Yangtze Craton, South China and correlations with other continents: evidence for a mantle superplume that broke up Rodinia. *Precambrian Res.* 122 (1), 85–109. [https://doi.org/10.1016/S0301-9268\(02\)00208-5](https://doi.org/10.1016/S0301-9268(02)00208-5).
- Li, Z., Liu, J., Li, Y., Hang, W., Hong, H., Ying, D., et al., 2015. Formation and evolution of Weiyuan-Anyue tensional corrosion trough in Sinian system, Sichuan Basin. *Pet. Explor. Dev.* 42 (1), 29–36. [https://doi.org/10.1016/S1876-3804\(15\)60003-9](https://doi.org/10.1016/S1876-3804(15)60003-9).
- Li, B., Fu, J., Qi, F., Tang, Y., 2017. Well Pad Drilling Technology in the Weiyuan Shale Gas Block. *Petrol. Drilling Techniques*. <https://doi.org/10.11911/syztjs.201705003>.
- Liang, X., Liu, S., Wang, S., Deng, B., Zhou, S., Ma, W., 2019. Analysis of the Oldest Carbonate Gas Reservoir in China—New Geological significance of the Dengying Gas Reservoir in the Weiyuan Structure, Sichuan Basin. *J. Earth Sci.* 30 (2), 348–366. <https://doi.org/10.1007/s12583-017-0962-y>.
- Liu, S., Yang, Y., Deng, B., Zhong, Y., Wen, L., Sun, W., et al., 2021. Tectonic evolution of the Sichuan Basin, Southwest China. *Earth Sci. Rev.* 213 <https://doi.org/10.1016/j.earscirev.2020.103470>.
- Ma, C., Zhang, X., Li, S., 2017. 3D geological modeling of effective shale-gas reservoirs: taking Wei 202H2 platform of Weiyuan area as an example. *Fault Block Oil Gas Field* 24, 495–499 in Chinese.
- Ma, X., Li, X., Liang, F., Wan, Y., Shi, Q., Wang, Y., et al., 2020. Dominating factors on well productivity and development strategies optimization in Weiyuan shale gas play, Sichuan Basin, SW China. *Pet. Explor. Dev.* 47 (3), 594–602. [https://doi.org/10.1016/S1876-3804\(20\)60076-3](https://doi.org/10.1016/S1876-3804(20)60076-3).
- Mahani, A.B., Schultz, R., Kao, H., Walker, D., Johnson, J., Salas, C., 2017. Fluid Injection and Seismic activity in the Northern Montney Play, British Columbia, Canada, with special Reference to the 17 August 2015 Mw 4.6 Induced Earthquake. *Bull. Seismol. Soc. Am.* 107 (2), 542–552. <https://doi.org/10.1785/0120160175>.
- McGarr, A., 2014. Maximum magnitude earthquakes induced by fluid injection. *J. Geophys. Res. Solid Earth* 119 (2), 1008–1019. <https://doi.org/10.1002/2013JB010597>.
- Meng, X., Chen, H., Niu, F., Tang, Y., Yin, C., & Wu, F., 2018. Microseismic monitoring of Stimulating Shale Gas Reservoir in SW China: 2. Spatial Clustering Controlled by the Preexisting Faults and Fractures. *J. Geophys. Res. Solid Earth* 123 (2), 1659–1672. <https://doi.org/10.1002/2017jb014491>.
- Richardson, N.J., Densmore, A.L., Seward, D., Fowler, A., Wipf, M., Ellis, M.A., et al., 2008. Extraordinary denudation in the Sichuan Basin: Insights from low-temperature thermochronology adjacent to the eastern margin of the Tibetan Plateau. *J. Geophys. Res. Solid Earth* 113 (B4).
- Rubinstein, J.L., Mahani, A.B., 2015. Myths and Facts on Wastewater Injection, Hydraulic Fracturing, Enhanced Oil Recovery, and Induced Seismicity. *Seismol. Res. Lett.* 86 (4), 1060–1067. <https://doi.org/10.1785/0220150067>.
- Schultz, R., Mei, S., Paná, D., Stern, V., Gu, Y.J., Kim, A., Eaton, D., 2015. The Cardston Earthquake Swarm and Hydraulic Fracturing of the Exshaw Formation (Alberta Bakken Play). *Bull. Seismol. Soc. Am.* 105 (6), 2871–2884. <https://doi.org/10.1785/0120150131>.
- Schultz, R., Skoumal, R.J., Brudzinski, M.R., Eaton, D., Baptie, B., Ellsworth, W., 2020. Hydraulic Fracturing-Induced Seismicity. *Rev. Geophys.* 58, 3. <https://doi.org/10.1029/2019rg000695>.
- Shearer, P.M., 1988. Cracked media, Poisson's ratio and the structure of the upper oceanic crust. *Geophys. J. Int.* 92 (2), 357–362. <https://doi.org/10.1111/j.1365-246X.1988.tb01149.x>.
- Sheng, M., Chu, R., Ni, S., Wang, Y., Jiang, L., Yang, H., 2020. Source Parameters of three Moderate size Earthquakes in Weiyuan, China, and their Relations to Shale Gas Hydraulic Fracturing. *J. Geophys. Res. Solid Earth* 125 (10). <https://doi.org/10.1029/2020jb019932>.
- Sheng, M., Chu, R., Peng, Z., Wei, Z., Zeng, X., Wang, Q., Wang, Y., 2022. Earthquakes Triggered by Fluid Diffusion and Boosted by Fault Reactivation in Weiyuan, China due to Hydraulic Fracturing. *J. Geophys. Res. Solid Earth* 127 (5). <https://doi.org/10.1029/2021JB022963>.
- Takei, Y., 2002. Effect of pore geometry on VP/VS: from equilibrium geometry to crack. *J. Geophys. Res. Solid Earth* 107 (B2). <https://doi.org/10.1029/2001JB000522>. ECV 6-1-ECV 6-12.
- Tan, Y., Hu, J., Zhang, H., Chen, Y., Qian, J., Wang, Q., et al., 2019. Hydraulic Fracturing Induced Seismicity in the Southern Sichuan Basin due to Fluid Diffusion Inferred from Seismic and Injection Data Analysis. *Geophys. Res. Lett.* 47 (4) <https://doi.org/10.1029/2019GL084885> e2019GL084885.
- Waldhauser, F., Ellsworth, W.L., 2000. A Double-Difference Earthquake Location Algorithm: Method and Application to the Northern Hayward Fault, California. *Bull. Seismol. Soc. Am.* 90, 1353–1368. <https://doi.org/10.1785/0120000006>.
- Wang, M., Shen, Z., 2020. Present-day crustal deformation of continental China derived from GPS and its tectonic implications. *J. Geophys. Res. Solid Earth* 125 (2). <https://doi.org/10.1029/2019JB018774>.
- Wang, M., Yang, H., Fang, L., Han, L., Jia, D., Jiang, D., Yan, B., 2020. Shallow Faults Reactivated by Hydraulic Fracturing: The 2019 Weiyuan Earthquake Sequences in Sichuan. *Seismological Research Letters*, China. <https://doi.org/10.1785/0220200174>.
- Wang, S., Jiang, G., Lei, X., Barbour, A.J., Tan, X., Xu, C., Xu, X., 2022. Three Mw \geq 4.7 Earthquakes within the Changing (China) Shale Gas Field Ruptured Shallow Faults Intersecting with Hydraulic Fracturing Wells. *J. Geophys. Res. Solid Earth* 127 (2). <https://doi.org/10.1029/2021JB022946>.
- Wei, Z., Chu, R., Xie, J., Bao, F., Zeng, S., Sheng, M., Zeng, Q., 2022. Crustal structure in the Weiyuan shale gas field, China, and its tectonic implications. *Tectonophysics* 837, 229449. <https://doi.org/10.1016/j.tecto.2022.229449>.
- Wells, D.L., Coppersmith, K.J., 1994. New empirical relationships among magnitude, rupture length, rupture width, rupture area, and surface displacement. *Bull. Seismol. Soc. Am.* 84 (4), 974–1002. <https://doi.org/10.1785/BSSA0840040974>.
- Wessel, P., Luis, J., Uieda, L., Scharroo, R., Wobbe, F., Smith, W., Tian, D., 2019. The generic mapping tools version 6. *Geochem. Geophys. Geosyst.* 20 (11), 5556–5564. <https://doi.org/10.1029/2019GC008515>.
- Wiemer, S., 2001. A Software Package to Analyze Seismicity: ZMAP. *Seismol. Res. Lett.* 72 (3), 373–382. <https://doi.org/10.1785/gssrl.72.3.373>.
- Yang, H., Zhu, L., Chu, R., 2009. Fault-Plane Determination of the 18 April 2008 Mount Carmel, Illinois, earthquake by Detecting and Relocating aftershocks. *Bull. Seismol. Soc. Am.* 99 (6), 3413–3420. <https://doi.org/10.1785/0120090038>.
- Yang, H., Liu, Y., Wei, M., Zhuang, J., Zhou, S., 2017. Induced earthquakes in the development of unconventional energy resources. *Sci. China Earth Sci.* 60 (9), 1632–1644. <https://doi.org/10.1007/s11430-017-9063-0>.
- Yang, H., Yao, S., He, B., Newman, A.V., 2019. Earthquake rupture dependence on hypocentral location along the Nicoya Peninsula subduction megathrust. *Earth Planet. Sci. Lett.* 520, 10–17. <https://doi.org/10.1016/j.epsl.2019.05.030>.
- Yang, H., Zhou, P., Fang, N., Zhu, G., Xu, W., Su, J., Meng, F., Chu, R., 2020. A shallow shock: the 25th February 2019 M_L 4.9 earthquake in the Weiyuan shale gas field in Sichuan, China. *Seismol. Res. Lett.* 91 (6), 3182–3194. <https://doi.org/10.1785/0220200202>.
- Yao, S., Yang, H., 2022. Hypocentral dependent shallow slip distribution and rupture extents along a strike-slip fault. *Earth Planet. Sci. Lett.* 578, 117296 <https://doi.org/10.1016/j.epsl.2021.117296>.
- Yi, G., Long, F., Liang, M., Zhao, M., Wang, S., 2020. Geometry and tectonic deformation of seismogenic structures in the Rongxian-Weiyuan-Zizhong region, Sichuan Basin: insights from focal mechanism solutions. *Chin. J. Geophys.* 63 (9), 3275–3291. <https://doi.org/10.6038/cjg20200095> in Chinese.
- Zelt, C.A., 1998. Lateral velocity resolution from three-dimensional seismic refraction data. *Geophys. J. Int.* 135 (3), 1101–1112. <https://doi.org/10.1046/j.1365-246X.1998.00695.x>.
- Zeng, Q., Chu, R., Sheng, M., Wei, Z., 2020. Seismic ambient noise tomography for shallow velocity structures beneath Weiyuan, Sichuan. *Chin. J. Geophys.* 63 (3), 944–955. <https://doi.org/10.6038/cjg2020N0177> in Chinese.
- Zhang, H., Thurber, C., 2006. Development and applications of Double-difference Seismic Tomography. *Pure Appl. Geophys.* 163 (2–3), 373–403. <https://doi.org/10.1007/s00024-005-0021-y>.
- Zhang, P., Deng, Q., Zhang, Z., Li, H., 2013. Active faults, earthquake hazards and associated geodynamic processes in continental China. *Scientia Sinica Terrae* 43, 1607–1620. In Chinese.
- Zhang, M., Ellsworth, W.L., Beroza, G.C., 2019. Rapid Earthquake Association and Location. *Seismol. Res. Lett.* 90 (6), 2276–2284. <https://doi.org/10.1785/0220190052>.
- Zhou, P., Yang, H., Wang, B., Zhuang, J., 2019. Seismological Investigation of Induced Earthquakes near the Hutubi Underground Gas Storage Facility. *J. Geophys. Res. Solid Earth* 124. <https://doi.org/10.1029/2019JB017360>.
- Zhao, Y., Jiang, G., Lei, X., Xu, C., Zhao, B., Qiao, X., 2023. The 2021 Ms 6.0 Luxian (China) earthquake: Blind reverse-fault rupture in deep sedimentary formations likely induced by pressure perturbation from hydraulic fracturing. *Geophys. Res. Lett.* 50, e2023GL103209. <https://doi.org/10.1029/2023GL103209>.
- Zhou, P., Ellsworth, W.L., Yang, H., Tan, Y.J., Beroza, G.C., Sheng, M., Chu, R., 2021. Machine-learning-facilitated earthquake and anthropogenic source detections near the Weiyuan Shale Gas Blocks, Sichuan, China. *Earth and Planetary Physics* 5 (6). <https://doi.org/10.26464/ep2021053>.

- Zhu, W., Beroza, G.C., 2018. PhaseNet: a deep-neural-network-based seismic arrival-time picking method. *Geophys. J. Int.* 216 (1), 261–273. <https://doi.org/10.1093/gji/ggy423>.
- Zhu, G., Wiens, D.A., Yang, H., Lin, J., Xu, M., You, Q., 2021. Upper Mantle Hydration Indicated by Decreased Shear Velocity near the Southern Mariana Trench from Rayleigh Wave Tomography. *Geophys. Res. Lett.* 48 (15) <https://doi.org/10.1029/2021GL093309>.
- Zi, J., Jia, D., Wei, G., Yang, Z., Zhang, Y., Hu, J., Shen, S., 2017. LA-ICP-MS U-Pb zircon ages of volcanoclastic beds of the third member of the Sinian (Ediacaran) Dengying formation in Leshan, Sichuan, and a discussion on the rift evolution in the basin. *Geol. Rev.* 63 (4), 10 in Chinese.